

Modelling the Thermal Structure and Circulations of Lake Nam Co, Central Tibetan Plateau

Yang Wu¹, Anning Huang², Youyu Lu³, La Zhu⁴, Bo Qiu⁵, Zhiqi Zhang⁶, and Xindan Zhang⁷

¹CMA-NJU Joint Laboratory for Climate Prediction Studies, School of Atmospheric Sciences, Nanjing University

²CMA-NJU Joint Laboratory for Climate Prediction Studies and State Key Laboratory of Severe Weather and Joint Center for Atmospheric Radar Research of CMA/NJU, School of Atmospheric Sciences, Nanjing University, Nanjing, 210023, China

³Bedford Institute of Oceanography

⁴Chinese Academy of Sciences

⁵Nanjing University

⁶CMA-NJU Joint Laboratory for Climate Prediction Studies and State Key Laboratory of Severe Weather and Joint Center for Atmospheric Radar Research of CMA/NJU, School of Atmospheric Sciences, Nanjing University

⁷MA-NJU Joint Laboratory for Climate Prediction Studies and State Key Laboratory of Severe Weather and Joint Center for Atmospheric Radar Research of CMA/NJU, School of Atmospheric Sciences, Nanjing University

November 26, 2022

Abstract

A three-dimensional (3-D) hydrodynamic model based on Princeton Ocean Model (POM) and a one-dimensional (1-D) lake model are applied to simulate the thermal structure and circulations of Lake Nam Co (LNC), the second largest lake in Tibet. Results show that POM can well reproduce the seasonal and synoptic variations of the in-situ observed vertical temperature profile, and the spatial distribution of satellite estimated lake surface temperature during May-December 2013. However, without considering the water and energy exchanges related to the lake hydrodynamics, the 1-D model exhibits much more evident biases in the lake thermal evolution. These shortages of the 1-D lake model solutions emphasize that the complex temperature-current interactions must be accounted for investigating the thermodynamics in large lakes over Tibet. From both observation and hydrodynamic simulations, LNC is identified to experience the springtime overturning, warm stratified phase during early-June to mid-November, autumnal overturning, and weak inverse stratified phase since mid-December. The two overturning processes last for about one month and are both related to the thermal bar development, which is controlled by the density-driven convection associated with the radiative heating (surface cooling) in spring (autumn). During the warm stratified phase, the eastern shallow basin is mainly characterized by anticyclonic circulation and bowl-shaped thermocline, while the central deep basin is featured by a cyclonic gyre (eastward currents) and dome-shaped (bowl-shaped) thermocline with the enhancement (weakness) of thermal stratification. The lake circulation during December is basically dominated by a single strong cyclonic gyre in the main lake basin.

Modelling the Thermal Structure and Circulations of Lake

Nam Co, Central Tibetan Plateau

Yang Wu^{1,2}, Anning Huang^{1,*}, Youyu Lu³, Lazhu⁴, Bo Qiu¹, Zhiqi Zhang¹,

Xindan Zhang^{1,2}

1. CMA-NJU Joint Laboratory for Climate Prediction Studies, School of Atmospheric

Sciences, Nanjing University, Nanjing, 210023, China

2. State Key Laboratory of Severe Weather and Joint Center for Atmospheric Radar

Research of CMA/NJU, School of Atmospheric Sciences, Nanjing University,

Nanjing, 210023, China

3. Fisheries and Oceans Canada, Bedford Institute of Oceanography, Dartmouth,

Nova Scotia, B2Y 4A2, Canada; Email: Youyu.Lu@dfo-mpo.gc.ca

4. Key Laboratory of Tibetan Environment Changes and Land Surface Processes,

Institute of Tibetan Plateau Research, Chinese Academy of Sciences, Beijing,

100101, China

Corresponding author:

Prof. Anning Huang, CMA-NJU Joint Laboratory for Climate Prediction Studies,

School of Atmospheric Sciences, Nanjing University, No.163 Xianlin Avenue, Nanjing,

Jiangsu, China, 210023. E-mail: anhuang@nju.edu.cn;

Abstract

A three-dimensional (3-D) hydrodynamic model based on Princeton Ocean Model (POM) and a one-dimensional (1-D) lake model are applied to simulate the thermal structure and circulations of Lake Nam Co (LNC), the second largest lake in Tibet. Results show that POM can well reproduce the seasonal and synoptic variations of the in-situ observed vertical temperature profile, and the spatial distribution of satellite estimated lake surface temperature during May-December 2013. However, without considering the water and energy exchanges related to the lake hydrodynamics, the 1-D model exhibits much more evident biases in the lake thermal evolution. These shortages of the 1-D lake model solutions emphasize that the complex temperature-current interactions must be accounted for investigating the thermodynamics in large lakes over Tibet. From both observation and hydrodynamic simulations, LNC is identified to experience the springtime overturning, warm stratified phase during early-June to mid-November, autumnal overturning, and weak inverse stratified phase since mid-December. The two overturning processes last for about one month and are both related to the thermal bar development, which is controlled by the density-driven convection associated with the radiative heating (surface cooling) in spring (autumn). During the warm stratified phase, the eastern shallow basin is mainly characterized by anticyclonic circulation and bowl-shaped thermocline, while the central deep basin is featured by a cyclonic gyre (eastward

39 currents) and dome-shaped (bowl-shaped) thermocline with the enhancement
40 (weakness) of thermal stratification. The lake circulation during December is basically
41 dominated by a single strong cyclonic gyre in the main lake basin.

42

43

44

45

46

47

48

49

50

51

52

53

1. Introduction

Lake-air interactions have been an important research hotspot in understanding the multiscale water and energy balances of the complex hydroclimatic systems (Sharma et al., 2018), especially over the lake-rich regions such as Tibetan Plateau (TP), which harbors the highest alpine lake concentrations among the world (Zhang, 2018). The total number and surface areas of the lake clusters distributed across TP exceed 1500 and 47000 km², respectively (Ma et al., 2011; Song et al., 2014). Such a huge amount of endorheic lakes exerts significant interactive impacts on the regional weather and climate by directly influencing the turbulent fluxes and the atmospheric boundary structure (Biermann et al., 2014; Zhu et al., 2017). Additionally, most TP lakes are continuously undergoing the rapid expansion processes (Guo et al., 2019; Zhang et al., 2017), which is closely associated with the glaciers retreat, permafrost degradation, and evaporation/rainfall variations under the background of the pronounced climate warming over TP (Wang et al., 2017b). All of these concerns have brought renewed attention to explore the thermal evolution regimes and hydrological cycling features of these TP lakes and their roles in the coupled lake-atmosphere ecosystem (Huang et al., 2017; Lei et al., 2014; Su et al., 2019; Wu et al., 2019; Yang et al., 2018).

During recent years, more field measurements and satellite observations are employed with various applications for exploring the complexities of TP lakes'

74 thermal features and understanding their impacts on the overlying atmosphere.
75 (Gerken et al., 2013a; Li et al., 2018; Liu et al., 2015; Qi et al., 2019; Wang et al.,
76 2015, 2017a; Wan et al., 2014). Based on the 2-yr in-situ water temperature records,
77 Wang et al. (2019) demonstrated that LNC, the second largest lake in central TP, is a
78 typical dimictic lake with different evolution of thermal stratification within its main
79 and eastern small basins. The different stratified structures are speculated to be
80 attributed to the distinctive spatial variability of heat capacity, which is modulated by
81 the lake morphometry (i.e. basin size, lake depth, and water volume) and water
82 transparency. Analogous summer thermocline developments are also observed in
83 many other high-altitude dimictic or meromictic TP lakes, i.e. Lake Bangong Co,
84 Lake Puma YumCo, Lake Dagze Co, and Lake Tangra YumCo (Murakami et al., 2007;
85 Wang et al., 2010; Wang et al., 2014). Due to the active lake-air interaction at
86 multi-timescales, the TP lakes are documented as the important moisture sources for
87 the low-level atmosphere and play critical roles in modulating the turbulent heat
88 fluxes and therefore the atmospheric boundary stability. For example, the evaporation
89 of LNC accounts for approximate 30% of the local atmospheric water vapor and
90 favors for the abundant convection during summer monsoon periods (Xu et al., 2011;
91 Haginoya et al., 2009), which is also the analogous situation for Lake Qinghai and
92 Erhai Lake (Cui and Li 2014; Haginoya et al., 2012). Throughout the ice-free period
93 of Lake Ngoring, the biggest freshwater lake in the Yellow River source region, the

94 positive lake-air temperature differences lead to the vast upward sensible/latent heat
95 fluxes and favors to maintain the persistent unstable atmospheric boundary layer (Li
96 et al., [2015](#)).

97 To make up the temporal discontinuity and spatial scarcity of observational data,
98 numerical models have been recently adopted as effective tools for systematically
99 assessing and gaining more insights into the interactions between TP lake
100 thermodynamics and the atmospheric conditions (Ao et al., [2018](#); Dai et al., [2018a](#);
101 Lazhu et al., [2016](#); Zhang et al., [2016](#)). By adopting the air-lake coupled Weather
102 Research and Forecasting Model (WRF), Wu et al. ([2019](#)) reveals that due to the
103 warming (cooling) lag effects induced by the large water thermal inertia, most lakes in
104 the southeastern central TP exhibit significant daytime cooling (nighttime warming)
105 effects on the overlying atmosphere, and thus dampen the diurnal variations of 2-m air
106 temperature. During daytime (nighttime), the lake-land thermal contrast related to the
107 colder (warmer) water surfaces over LNC tends to generate over-lake divergent
108 (convergent) airflow, which would further interact with the valley (mountain) breeze
109 to suppress (stimulate) the convective activities over and downstream the lake
110 (Gerken et al., [2013b](#); Yang et al., [2015](#)). At the seasonal time scale, the Ngoring and
111 Gayring Lake are found to decrease the air temperature variability and promote more
112 nighttime convective rainfall during July to October (Wen et al., [2015](#)). Xu et al.

113 (2019) demonstrated that Erhai lake has predominant impacts on decreasing
114 (increasing) air temperature and atmospheric boundary layer height during daytime
115 (nighttime), and the local circulations therein can be fully developed throughout the
116 pre-monsoon period.

117 To date, the aforementioned offline or coupled representations of the TP lake
118 thermodynamics are all accomplished by one-dimensional (1-D) lake models, i.e. the
119 Freshwater Model based on self-similarity theory (Mironov 2008) or the Hostetler
120 model with parameterized wind-driven eddy thermal diffusion (Hostetler et al., 1993;
121 Subin et al., 2012). The above 1-D lake models are all designed with different
122 physical concepts and varying levels of simplification in lake processes. During recent
123 years, considerable calibrations of keyparameters including water/ice albedo, light
124 attenuation coefficient, surface roughness length, and vertical mixing
125 parameterization have been proceeded to refine the 1-D lake models' performance in
126 depicting the diurnal/seasonal characteristics of turbulent lake-air heat exchanges and
127 the lake thermodynamics (Dai et al., 2018b; Huang et al., 2019; Kirillin et al., 2017;
128 Wen et al. 2016; Xu et al., 2015). However, there still exist large disadvantages for the
129 1-D lake models to realistically capture the thermal bar formation, springtime lake
130 warming processes, summer dome/bowl-shaped thermocline, and
131 destratification/overturning characteristics in autumn-winter for large thermally

132 stratified lakes (Bennington et al., [2014](#); Martynov et al., [2010](#); Notaro et al., [2013](#);
133 Xiao et al., [2016](#)). These unsatisfactory model discrepancies imply that in addition to
134 the local-scale lake-air feedback or oversimplified vertical thermodynamics resolved
135 by the 1-D lake models, a comprehensive representation of three dimensional (3-D)
136 temperature-current interactions must be accounted for better simulating the energy
137 redistribution within lakes and thus the evolution features of the limnological
138 phenomena mentioned above. Specifically, a nearshore-offshore temperature gradient
139 that is commonly stimulated by the differential heating rate between the shallower
140 coastal and deeper mid-lake regions (Monismith et al., [1990](#)) could last for several
141 months in large deep lake systems (Blokhuin and Selin, [2019](#)). Such persistent
142 thermal gradients can not only directly affect the advective heat transport across the
143 thermal front, but also work in concert with the Coriolis force and wind stress to
144 determine the water currents, both of which lead to the lake mixing processes much
145 more complicated (Beletsky et al., [2012](#); Huang et al., [2010](#); Rao and Schwab [2007](#);
146 Xue et al., [2015](#)). Besides, the wind-wave-induced Langmuir circulation and the
147 Ekman pumping transport associated with the wind stress vorticity can also jointly
148 modify the 3-D lake circulation and heat transport (Aijaz et al., [2017](#); Bennington et
149 al., [2010](#); Gill [1982](#)). These complex mixing processes related to the basin-scale or
150 local-scale gyres/currents driven by the baroclinic stratification and wind stress curl
151 are missing in 1-D lake models, where the mixing adjustment is simplified as vertical

152 and determined by the wind speed and convective instability (Gu et al., 2015). The
153 inadequate physical representations would ultimately worsen the model performances
154 in simulating the spatiotemporal variations of large-lake thermodynamics (Leon et al.,
155 2007; Long et al., 2007; Xue et al., 2016). The comparisons between the 1-D lake-air
156 coupled model simulations and 3-D lake-air coupled model simulations on the Lake
157 Victoria further confirm that precluding the flow-dependent heat transport from the
158 heat surplus regions to cold regions directly leads to the degraded simulation in both
159 the surface water temperature pattern and the lake-effected wind/rainfall fields over
160 and downstream the lake areas (Song et al., 2004; Sun et al., 2014). All of these
161 research concerns have pointed to the issue that due to the absence in the
162 representation of lake hydrodynamics, the current applications of 1-D lake models to
163 the large deep lakes over TP would suffer from inevitable degraded performances in
164 simulating the lake thermodynamics and their impacts on regional climate.

165 Recent studies based on the high-resolution remote sensing data have revealed
166 that the Qinghai Lake, Lake Siling Co, and LNC are characterized by large surface
167 areas and complex bathymetry/geometry, and they all exhibit apparent spatial
168 variability in surface water temperature (Ke and Song, 2014; Lu et al., 2019; Xiao et
169 al., 2013), which reflect the interactions between the thermohydrodynamics of large
170 lakes and the overlying atmosphere. Hence, to reveal much more detailed thermal

171 structures of these TP lakes, we should adopt 3-D hydrodynamic models rather than
172 the most commonly used 1-D lake models, i.e. the Hostetler-based lake component
173 from WRF (WRF-Lake) that has been widely applied for offline/coupled studies on
174 TP lakes (Xu et al., 2016; Zhu et al., 2017; Zhang et al., 2018; Huang et al., 2019; Wu
175 et al., 2019). Based on the valuable 1-yr in-situ water temperature records of LNC, the
176 second largest lake in central TP, the main goals of this study are: (1) to explore the
177 superiority of the 3-D hydrodynamic lake model based on the Princeton Ocean Model
178 (POM) in reproducing the large-lake thermodynamics during May-December than the
179 1-D WRF-Lake model; (2) to present the 3-D evolution features of thermal structures
180 and hydraulic currents in LNC for the first time. Main findings of this study may help
181 to explain the present shortcomings in the 1-D lake modeling and could provide
182 valuable backgrounds for fully coupling 3-D lake models with atmospheric models to
183 reveal the lake-air interactions over the large lakes of TP.

184 The rest of this paper is organized as follows. In Section 2, we describe the
185 forcing and validation datasets, the configurations of POM and WRF-Lake, numerical
186 experimental design, and the methodology used in this study. Model comparisons in
187 reproducing the lake surface temperature and water temperature profile are
188 systematically analyzed in Section 3.1. Section 3.2 presents the detailed 3-D thermal
189 structure and circulations in LNC. Finally, summary and discussion are given in

190 Section 4.

191 **2. Datasets, Model Description and Experimental Design, and Methodology**

192 **2.1 Datasets**

193 LNC situates at the northeastern edge of the elevated Nyainqentanglha Mountain,
194 central TP (Figure 1a). It extends from 30°30'N to 30°55'N and 90°16'E to 91°03'E,
195 and has a large surface area exceeding 2000 km² and a maximal depth of 98.9 m in its
196 central basin (Wang et al., 2009, 2019). In 2013, two sets of in-situ observations of
197 weather conditions and the lake water temperature profiles were made and these data
198 are used for model initialization and assessments. The daily meteorological variables,
199 i.e., the surface solar radiation, surface downward longwave radiation, relative
200 humidity at 10 m above ground, air temperature at 2 m above ground, and surface
201 pressure and wind speed were collected by an automatic weather station located
202 approximately 1.5 km from the southeastern shoreline of LNC (red aster in Figure 1b).
203 The daily lake water temperature profile, sampled at depths of 3, 6, 16, 21, 31, 36, 56,
204 66, and 83 m, was measured at the site indicated by the purple aster in Figure 1b
205 (Lazhu et al., 2016). In addition, the MODIS product (MOD11A1), with a spatial
206 resolution of 1 km, provides the instantaneous remote-sensing lake surface temperature
207 (LST) imagery at approximately 11:00 and 21:00 local time over LNC (available at
208 <https://modis.gsfc.nasa.gov/data/dataproduct/mod11.php>; Wan et al., 2004).

209 The model simulations cover 1th May to 31th December 2013. The atmospheric

210 forcing inputs include the air temperature at 2 m height, surface pressure, specific
211 humidity and wind speed at 10 m height, and surface downward shortwave and
212 longwave radiation. These input data are mainly derived from the long-term
213 (1979-2018) China Meteorological Forcing Dataset (CMFD) with a temporal
214 resolution of 3 hours and a horizontal resolution of 0.1° (available at
215 <http://en.tpdatabase.cn/portal>; He et al., 2020). CMFD is produced through
216 assimilating vast amounts of ground-based observations besides several
217 remote-sensing and reanalysis datasets, and it is documented to be a superior
218 near-surface meteorological data for land surface process and hydrology researches
219 over China (Chen et al., 2011; Huang et al., 2017, 2019). Comparison with the in-situ
220 weather station data (Figure 2) demonstrates that CMFD can well represent the daily
221 variations of the over-lake meteorological variables except for an overall
222 underestimation of the wind speed, especially during fall-winter (September to
223 December). Following Lazhu et al (2016), the CMFD wind speed is calibrated using the
224 piecewise linear regression relationships between the daily CMFD and in-situ weather
225 station wind speed established for spring-summer (May to August) and fall-winter,
226 respectively (Figure 2e). The wind direction, which is not available in CMFD, is
227 derived from the contemporarily up-to-date hourly ERA5_Land reanalysis with a
228 horizontal resolution of 9 km (available at <https://cds.climate.copernicus.eu>;
229 Copernicus Climate Change Service 2019).

2.2 Model Description and Experimental Design

The 3-D coastal ocean model POM solves nonlinear governing equations of lake water motions based on hydrostatic and Boussinesq approximations using finite difference method (Blumberg and Mellor 1987). The horizontal space is discretized with a uniform grid spacing of 1 km, and the vertical discretization uses 31 terrain-following sigma levels with finer resolution near the surface/bottom. The centers of the sigma levels are located at -0.0005, -0.002, -0.0055, -0.009, -0.0155, -0.026, -0.0365, -0.047, -0.0575, -0.068, -0.0785, -0.089, -0.0995, -0.11, -0.1205, -0.131, -0.1415, -0.152, -0.1625, -0.173, -0.1835, -0.194, -0.2045, -0.262, -0.3715, -0.486, -0.6, -0.714, -0.883, -0.9975. The Mellor and Yamada (1982) level 2.5 turbulence closure scheme (MY-2.5) and the Smagorinsky eddy parameterization with a multiplier of 0.2 are employed to calculate the vertical and horizontal mixing coefficients, respectively. The lake water has no exchange of heat with the closed lateral boundaries and lake bottom. The velocity is free-slip along the lateral boundaries, and the friction at the lake bottom is parameterized in quadratic form with the drag coefficient calculated according to:

$$C_{db} = \max \left[\frac{\kappa^2}{\ln(z_b/z_{0b})^2}, 0.0025 \right] \quad (1)$$

where $\kappa = 0.41$ is the von Karman constant, z_b is the distance from the bottom to the bottom layer center, and $z_{0b} = 0.01 \text{ m}$ is the bottom roughness length.

Time-independent forcing is applied at lake surface. The downward shortwave radiation (SW_{\downarrow}) and longwave radiation (LW_{\downarrow}) are specified according to CMFD, and 40% (60%) of the shortwave radiation are accounted by the infrared (visual) band, with the vertical extinction coefficient assumed as 2.85 (0.1) m^{-1} . The surface wind stress is calculated according to:

$$(\tau_x, \tau_y) = \rho_a C_d(u, v) \sqrt{u^2 + v^2} \quad (2)$$

where τ_x, u (τ_y, v) are the east-west (north-south) component of surface wind stress ($\text{N} \cdot \text{m}^{-2}$) and wind speed at 10 m height (ms^{-1}), $\rho_a = 100P_a/R_a(273.15 + T_a)$ is the moist air density ($\text{kg} \cdot \text{m}^{-3}$), P_a is the input surface air pressure (hPa), $C_d = (7.5 + 0.67\sqrt{u^2 + v^2}) \times 10^{-4}$ is the wind drag coefficient (Garratt, 1977). The upward longwave (LW_{\uparrow}), sensible (SH_{\uparrow}) and latent (LH_{\uparrow}) heat fluxes are calculated based on the prognostic water surface temperature. The dynamic lake-air interactions are included in the computed heat fluxes, and this has advantages over the prescribed or precomputed surface heat fluxes (Xue et al., 2015). The equation for LW_{\uparrow} and the bulk aerodynamic formulae for SH and LH (Verburg and Antenucci 2010) are:

$$LW_{\uparrow} = \varepsilon \sigma T_w^4 \quad (3)$$

$$SH_{\uparrow} = \rho_a C_{pa} C_{sh}(T_w - T_a) \sqrt{u^2 + v^2} \quad (4)$$

$$LH_{\uparrow} = \lambda_v \rho_a C_{lh}(q_w - q_a) \sqrt{u^2 + v^2} \quad (5)$$

263 where $\varepsilon = 0.98$ is the lake surface emissivity, $\sigma = 5.67 \times 10^{-8} \text{ W} \cdot \text{m}^{-2} \cdot \text{K}^{-4}$ is
264 the Stefan-Boltzmann constant, T_w (T_a) (in K) is the surface water (air) temperature,
265 $R_a = 287(1 + 0.608q_a)$ (in $\text{J} \cdot \text{kg}^{-1} \cdot \text{K}^{-1}$) is the gas constant for moist air, $C_{pa} = 1005$
266 $\text{J} \cdot \text{kg}^{-1} \cdot \text{K}^{-1}$ is the specific heat of air, $C_{sh} = 0.0001$ ($C_{lh} = 0.00016$) is the bulk
267 constant coefficient of sensible (latent) heat, $\lambda_v = 2.501 \times 10^6 - 2370(T_a -$
268 $273.15)$ is the latent of vaporization, and q_a (q_w) (in $\text{kg} \cdot \text{kg}^{-1}$) is the (saturated)
269 specific humidity. For all the above heat flux components, positive (negative) values
270 mean that the lake water loses (gains) heat from the atmosphere.

271 The version of POM used for the present study does not include an ice
272 component. Hence, the simulation is carried out from 1th May 2013 to 31st December
273 2013 to avoid dealing with the season with significant ice cover from January to April
274 (Gou et al., 2017). POM is initialized with zero currents, a constant salinity of 1.7 g L^{-1} ,
275 and a uniform temperature of 1.96°C , which is the depth-averaged value of the rather
276 homogeneous lake water temperature at 1th May 2013 according to in-situ
277 observations.

278 Besides POM, the 1-D lake component in the Weather Research and Forecasting
279 Model (WRF-Lake), which solves the snow, lake water/ice, and soil sediment processes
280 within a lake column, is also used. Detailed model descriptions can be found in Gu et al.
281 (2015). WRF-Lake has undergone significant model process calibrations and has been

282 extensively applied in simulating the lake thermodynamics for various offline/coupled
283 applications (Huang et al., 2019; Wang et al., 2019; Wu et al., 2019, manuscript
284 submitted to *Clim. Dyn.*; Xu et al., 2016). In this study, the 1-D WRF-Lake with 25
285 vertical lake layers is solved for each horizontal grid of POM for the same 8-month
286 period. Using the same initial conditions and surface forcing as used by POM, 1-D
287 WRF-Lake gives a 3-D thermal representation of LNC for comparison with the POM
288 simulation. Additionally, we conducted a series of sensitivity experiments and
289 introduced adjustments to several key parameters, i.e. a parameterized surface
290 roughness length (Subin et al., 2012), realistic temperature of maximum water density
291 ($T_{dmax}=3.5^{\circ}\text{C}$), and a decreased light extinction coefficient with a scale factor of 0.8,
292 to obtain the optimal WRF-Lake results for comparison.

293 **2.3 Methodology**

294 For comparisons with the in-situ observations, the lake temperature profiles
295 simulated by POM and WRF-Lake at the observation site are selected and linearly
296 interpolated onto the observed layers. The bimonthly MODIS and model simulated
297 LST are processed following two steps. First, for each MODIS imagery, the values on
298 the pixels located within the lake model domain (Figure 1b) are extracted. Because
299 POM does not contain an ice component, the nearshore MODIS pixels with LST
300 values less than 0°C are excluded. Second, the selected MODIS data are interpolated
301 onto the model grids with the bilinear interpolation method (Shepard 1968). The

302 gridded MODIS LST can then be compared with the model results at bimonthly
 303 intervals. The assessment uses four statistical parameters, i.e., the mean bias (BIAS),
 304 root-mean-square error (RMSE), Pearson temporal correlation (TC), and the Taylor
 305 score (TS), following Huang et al (2019).

306 The heat balance for the lake water column in a given time interval can be
 307 expressed as (Wetzel and Likens 2000; Titzel and Austin 2014):

$$\frac{\delta}{\delta t} LHC = SNHF + \theta_{hor} + \theta_{sed} \quad (6)$$

$$LHC = C_{pw} \rho_w \int_0^h T(z) dz \quad (7)$$

$$SNHF = SW_{\downarrow} + LW_{\downarrow} - LW_{\uparrow} - SH_{\uparrow} - LH_{\uparrow} \quad (8)$$

308 where $\delta LHC / \delta t$ ($\text{W} \cdot \text{m}^{-2}$) is the rate of heat content change within the lake column of
 309 unit area, which is balanced by the surface net heat flux ($SNHF$, $\text{W} \cdot \text{m}^{-2}$), horizontal
 310 heat transport due to advection and mixing (θ_{hor} , $\text{W} \cdot \text{m}^{-2}$), and the conductive heat
 311 exchange between lake water and bottom sediments. $C_{pw} = 4180 \text{ J} \cdot \text{kg}^{-1} \cdot \text{K}^{-1}$ is the
 312 specific heat of water, $\rho_w = 1000 \text{ kg} \cdot \text{m}^{-3}$ is the water density, h is the bottom lake
 313 depth, $T(z)$ (in $^{\circ}\text{C}$) is the lake temperature at depth z (in m). Note that $\theta_{hor} = 0$ for
 314 the 1-D WRF-Lake model, and can be estimated as $\delta LHC / \delta t - (LHC + SNHF)$ in
 315 POM due to the adiabatic bottom boundary conditions. Positive $SNHF$ and θ_{hor}
 316 mean that the lake column gains heat. The above heat budget components are firstly

317 calculated based on the daily POM results and are then analyzed for bimonthly
318 intervals for representations. The heat budget analysis is not performed for
319 November-December due to the missing solution of ice thermodynamics in POM.

320 **3. Results**

321 **3.1 Model Comparisons: Surface Layer Temperature and Lake Water** 322 **Temperature Profile**

323 **3.1.1 Surface Layer Temperature**

324 Figure 3 gives the in-situ observed and simulated daily time series of the lake
325 temperature at 3-m depth (TLake_{3m}), and Figure 4 presents the related quantitative
326 statistics at both daily and bimonthly timescales to evaluate the abilities of POM and
327 WRF-Lake in reproducing the lake surface layer temperature. Since 1th May 2013, the
328 TLake_{3m} at the Nam Co buoy exhibits a continuous warming tendency from 2°C to
329 11.9°C until late August and then gradually decreases to 1.35 °C at the end of
330 December (Figure 3). Although both POM and WRF-Lake generally reproduced the
331 daily TLake_{3m} variability with the TC/TS exceeding 0.95 (Figure 4), the 3-D lake
332 model POM shows preferable capabilities in the temporal evolution of TLake_{3m}
333 during May-December. Specifically, POM gives better representations in the rapid
334 lake warming process since early June, the gradual TLake_{3m} decrease during the
335 autumnal destratification period, and the synoptic cooling events under weak lake
336 stratification around mid-December, suggesting that POM can reasonably capture the

lake physical processes on seasonal and synoptic timescales. The 1-D WRF-Lake tends to underestimate the $TLake_{3m}$, especially for the lake destratification/overturning periods with the large negative BIAS of $-1.74 (-1.45) ^\circ C$ in September-October (November-December), while the $TLake_{3m}$ simulated by POM shows a slight warm BIAS (RMSE) of $0.2 (0.52) ^\circ C$ for the whole simulation period (Figure 4).

Figure 5 gives the spatial distribution of the bimonthly MODIS observed and POM/WRF-Lake simulated LST. Figures 6 and 7 present the bimonthly variations of heat budgets ($\delta LHC / \delta t, SNHF, \theta_{hor}$) simulated by POM over LNC and at the Nam Co water temperature site, respectively. With the intensified solar heating in May-June, LNC experienced the springtime warming process from its original thermally mixed state in pre-winter. The simultaneous lake column heat storage shows a general increase across the whole lake (Figure 6a). As the depth-influenced heat capacity increases from coastal to central lake regions, LST over the shallower areas rises with a faster rate in response to the radiative forcing. The horizontal nearshore-offshore temperature gradient forms basically across the isobath (Figures 5a-c), which is also documented in many other large deep lakes with sloping bottom bathymetry (Bai et al., 2013; Rao et al., 2004). This cross-isobath temperature gradient can not only enhance the horizontal temperature diffusion, but also stimulate

the vertical shear of the water flow through the thermal wind relation to form density-driven movements, both of which tend to redistribute the water/energy within the lake (Beletsky and Schwab 2001). During May-June, the surface currents in LNC consist of two contour-rotating gyres in response to the baroclinic and bathymetry effects (Figure 5b). As the cyclonic circulation in the main basin sustains the heat advection from the warm shore to the mid-lake areas (Figure 6c), the LST pattern simulated by POM is characterized by a less pronounced nearshore-offshore temperature gradient, and thus the ‘cold pool’ in the central deep lake is warmer than the 1-D WRF-Lake results (Figures 5b and c). At the Nam Co water temperature site, the horizontal heat exchanges contributes approximately 12% of the bimonthly increase rate in lake column heat storage (Figure 7), illustrating that the resolved flow-dependent heat transport plays an important role in POM for reproducing the more realistic LST warming strength during May-June relative to the 1-D WRF-Lake simulations. Accompanied by the persistent solar radiation heating and the water/energy transportation toward the basin center during July-August, the spatial variability of LST decreases and LNC gets fully stratified with a relatively homogeneous epilimnion (as seen for instance in the July-August plot of Figure 9). Lake circulations are dominated by anticyclonic motions in the eastern small basin and appear as regional cyclonic gyres in the main basin due to the stratification development (Figure 5e). Such hydrodynamic processes maintain the summertime

energy transport from heat surplus to colder deep regions and decrease the spatial variabilities of *LHC* change (Figures 6d-f). During July-August, the horizontal heat exchanges account for ~14% of the increase in lake column heat content at the in-situ station and favor for the satisfactory LST warming simulation by POM (Figures 3 and 7). In comparison with the bimonthly lake-averaged LST from MODIS products, both POM and WRF-Lake overestimate with a BIAS of 0.28 (0.83) °C and 0.3 (0.27) °C during May-June (July-August), respectively (Table 1). As reported by previous MODIS LST evaluation researches, the remote-sensed LST from satellites is usually lower than the in-situ measurements due to the cool skin effects, and the absolute BIAS against many other lake field observations is within the range of 0.8-1.9°C (Hook et al., 2003; Ke and Song 2014). Hence, we consider that both models exhibit good performances in qualitatively reproducing the lake-averaged LST during the spring-summer periods. However, the models' abilities in simulating the synchronous LST spatial distributions are hard to evaluate because the model BIAS and data uncertainties possess comparable magnitudes.

Driven by the strong winds and large positive lake-air temperature and humidity gradients during September-October, the over-lake turbulent sensible/latent heat fluxes increase rapidly and act a negative feedback on LST. The lake-averaged LST from MODIS (POM) experienced comparable cooling amplitudes from 10.74 (11.57)

395 °C in July-August to 9.38 (9.85) °C in September-October (Table 1). While, the
396 simultaneous LST modeled by WRF-Lake shows an excessive decrease of 2.79°C from
397 11.01°C to 8.20°C, which has been previously reported as the rapid autumnal cooling
398 issue in Hostetler model by Martynov et al (2010). LST from both MODIS and POM
399 presents a pronounced horizontal gradient increasing from northwest to southeast
400 (Figures 5g and h), which can be partly attributed to the eastward warm water
401 aggregation caused by the prevailing westerly wind, especially during October when
402 the lake circulation is largely influenced by the surface winds under weakly stratified
403 conditions (not shown). However, such LST spatial pattern cannot be well captured by
404 the 1-D WRF-Lake model, implying that the hydrodynamic processes besides the local
405 turbulent lake-air fluxes must be considered for redistributing energy and better
406 simulating the LST spatial variability over large deep-water bodies such as LNC.
407 During September-October, the horizontal energy transportation is basically from the
408 western coastal to central lake regions (Figures 6g-h). For the Nam Co water
409 temperature site, the eastward energy transport during this period tends to counteract
410 the significant *SNHF* loss and leads to the more realistic decrease rate of LST modeled
411 by POM compared to the 1-D WRF-Lake simulations (Figures 3 and 7). With the
412 progress of destratification and overturning processes during autumn-winter, the entire
413 water body temperature descends continuously with a slower LST decreasing rate over
414 central deep water regions, where the epilimnetic heat loss can be partly compensated

415 by the warm hypolimnion due to the wind-induced mixing or gravitationally-driven
416 vertical energy exchanges when the LST decreases to T_{dmax} . From MODIS products,
417 LST in the middle lake is approximately 1.5°C higher than that in the coastal areas
418 during November-December. Although both models present a warmer LST in middle
419 lake, the lake-averaged LST simulated by WRF-Lake is unrealistically lower than the
420 MODIS LST with a large BIAS of -2.6°C . The excessive LST decrease in the 1-D
421 WRF-Lake model can be attributed to the insufficient upward heat transport induced by
422 the unresolved Ekman upwelling and the less heat retention in the central lake regions
423 during previous spring-summer periods (Figures 5j-i). For the autumn-winter periods,
424 POM is evidently superior in modeling both the lake-averaged LST with much lower
425 BIAS/RMSE and the spatial distribution of LST compared with the WRF-Lake
426 simulations.

427 3.1.2 Vertical Temperature Profile

428 In this section, we assessed the seasonal variation of vertical temperature profile
429 modeled by POM and WRF-Lake against the field mooring observations. Figure 8
430 presents the time-depth distributions of the daily observed and modeled water
431 temperature during May-December, and Figure 9 quantitatively evaluates models'
432 performance in simulating the lake temperature at 10 observed layers. To indicate the
433 development of lake thermal stratification, we define the first/last date, from which the

434 temperature differences between 6-m and 66-m lake depth are greater than 1°C, as the
435 onset/end of lake thermal stratification (Wang et al., 2019).

436 From Figure 8a, the observed water column at the Nam Co buoy shows a small
437 negative temperature gradient from the lake surface to deeper layers until the lake
438 thermal stratification establishes at 4th June. As the result of the persistent radiative
439 heating during June to late September (Figures 2a and b), the vertical thermal
440 structure at this deep-water station is characterized by a rather homogeneous warm
441 epilimnion with its maximum depth exceeding 30m. Since then, the mean epilimnetic
442 temperature gradually descends to ~5.5°C due to the intensified surface heat flux loss
443 and vertical mixing strength, and the mixed layer depth finally reaches ~50m at the
444 end of destratification period (7th November). During the subsequent lake overturning
445 periods, the entire water body temperature experiences an almost uniform cooling
446 process before the LST approaches the T_{dmax} around mid-December, after which the
447 typical inverse thermal stratification begins to develop due to the density-driven
448 convection.

449 Both POM and WRF-Lake can generally reproduce the seasonal evolution of
450 thermal structures, especially for the pattern and amplitude of the subsurface (3-16m)
451 water temperature variability implied by the TC/TS greater than 0.9 (Figures 9a and c).
452 However, their capabilities in quantitatively simulating the stratification development

453 vary significantly and several discrepancies against field measurements are evident.
454 First, the establishment of thermal stratification modeled by POM (7th June) and
455 WRF-Lake (15th June) is somewhat postponed than the observations (4th June). POM
456 predicts the onset of stratification more accurately because the flow-dependent heat
457 transport from warm nearshore areas to Nam Co station is beneficial for an earlier
458 stratification development (Figure 6c and 7). Second, both models show degraded
459 performances in modeling the temperature of metalimnion, and the largest
460 discrepancies occur at the 21-m lake depth with a much smaller RMSE of 1.3°C from
461 POM than from WRF-Lake (2.38°C) (Figure 9b). In terms of the oscillating evolution
462 of thermocline displacements, POM also performs better than WRF-Lake despite with
463 some errors. For example, the mixed layer in POM is shallower and the thermocline is
464 more diffuse compared with the observations, which is consistent with the similar
465 issue reported by the previous POM applications on Lake Michigan and Lake Erie
466 (Beletsky et al., 2006, 2013). Additionally, during the late summer, POM fails to
467 capture the rapid thermocline jump episodes occurring at 21-31 m, where the short-term
468 temperatures were documented to exhibit large abrupt fluctuations exceeding 3°C due
469 to the intensive internal wave activities in the upper portion of thermocline (Wang et al.,
470 2019). These discrepancies, which can be attributed to both the wind fields
471 uncertainties and the current POM model's intrinsic defects including the absent
472 nonbreaking wave-induced mixing (i.e. Langmuir circulation), the numerical diffusion,

473 and the not fully resolved internal waves (Huang and Qiao, [2010](#); Kantha and Clayson
474 [2004](#)), are still challenging problems to overcome. Third, the destratification date
475 modeled by WRF-Lake (31th October) is earlier than the observation (7th November),
476 while it is delayed by about 2 weeks in the POM results (20th November). As previously
477 discussed in explaining the LST underestimation by WRF-Lake during autumn-winter
478 periods, the modeled earlier autumnal destratification and colder wintertime water
479 column temperature at this deep-water station are also the results of the less heat
480 retention and the missing horizontal energy exchanges. The postponed destratification
481 in POM points to the issue again that the current wind-wave-induced mixing strength
482 in POM is insufficient to describe the convection activities under both the strong and
483 weak stratified phases. This concern needs to be remedied before its coupling
484 application on exploring the ecological impacts of lake thermal stratification.

485 In summary, the 3-D POM shows much better ability than the 1-D WRF-Lake in
486 reproducing the seasonal and synoptic variations of LST and vertical thermal
487 structures. The RMSEs of the POM modeled water temperature at all of the 10
488 observed layers are within a reasonable range from 0.39°C to 1.3 °C (Figure [9b](#)). This
489 gives us confidence to present the 3-D thermal structure and circulations of LNC in the
490 following Section.

3.2 Three-Dimensional Thermal Structure and Circulations

As documented by previous studies, the temperature fields and current structure in large lake water bodies show pronounced spatiotemporal variability due to the multiscale thermohydrodynamics (Nyamweya et al., 2016; Xue et al. 2015, 2017). LNC is a large typical dimictic lake and features complex limnological phenomena during May-December, i.e. spring thermal bar, summertime stratification, autumnal destratification, and hibernal turnover processes (Wang et al., 2019), all of which significantly affect the natural/anthropogenic particle transport and the biota growth within the lake ecosystems. To broaden the knowledge about the thermodynamics of LNC from limited in-situ observations, we are going to utilize the POM results to obtain more specifics about the development of the 3-D lake thermal structure and circulations in the following part. Figures 10 and 11 present the lake temperature along a vertical southwest-northeast transection, the LST, and the depth-averaged water currents at monthly timescales.

For many large temperate lakes with sloping bottom bathymetry, the spring thermal state is mainly determined by an important limnological phenomenon namely “thermal bar”, which is defined as the water column with the temperature of T_{dmax} and serves as a barrier in separating the stratified nearshore waters and the thermally mixed central deep water areas (Rao et al., 2004; Tsydenov 2019). The spring thermal bar reflects the thermohydrodynamic processes in response to the radiative heating and

511 density-driven adjustment when the lake is heated convectively from cold water
512 temperature to T_{dmax} . The classical spring thermal bar development can also be
513 observed in LNC (Figures 10a and b). Firstly, due to the high altitude (4731m) and the
514 related cold air temperature over LNC during winter, the lake water temperature is
515 usually rather homogenous with a value less than 2°C before May. Such a low heat
516 retention in previous winter provides the essential prerequisites for the spring thermal
517 bar development. As the result of the intensified solar radiation from spring to early
518 summer and its depth-decayed penetrating features (Figures 2a and b), the upper water
519 body receives large portions of the incoming radiation and is heated towards T_{dmax} .
520 During this period, the denser epilimnion would continuously sink and mix with the
521 cold deeper water body, and thus the whole lake column temperature rises
522 homogeneously with a slow rate until the hypolimnetic temperature reaches T_{dmax} and
523 the stable density gradient forms. From then on, the epilimnetic temperature rises
524 rapidly due to the weakened top-to-bottom mixing, as can be indicated by the fast
525 $TLake_{3m}$ warming tendency at the Nam Co buoy since the onset of thermal
526 stratification (4th June) (Figures 3 and 8). A weak thermal stratification is firstly
527 established around the coastal regions of LNC in May, while the deep mid-lake regions
528 still experience the convective heating process due to the larger heat capacities (Figure
529 10a). There exists a narrow zone with typical converging flow patterns (namely thermal
530 bar), which divides the warm stratified nearshore and cold thermally homogeneous

531 offshore areas and inhibits the horizontal water/energy exchanges between them.
532 During this period, as the thermal bar hasn't reached the deep-water Nam Co buoy
533 (~93m), its water column is mainly characterized by the continuous
534 gravitationally-driven convection in response to the density inversion triggered by
535 radiative heating. Hence, the water column temperature at this station exhibits a slow
536 warming tendency (Figure 8) and the observed (POM modeled) T_{Lake_{3m}} rises weakly
537 from 1.99 (1.99) °C to 3.44 (3.21) °C during May (Figure 3). While, once the thermal
538 bar passes across the Nam Co buoy during its progressive movement from shoreline to
539 the deep mid-lake parts, the T_{Lake_{3m}} rises rapidly due to the weakened top-to-bottom
540 mixing and the horizontal heat transport from warm nearshore regions (Figures 3 and
541 6c), implying the establishment of thermal stratification at this water temperature site
542 (4th June as observed). POM gives a reasonable simulation in the onset of the stratified
543 phase at this in-situ site (7th June) and reveals that the thermal stratification in the
544 central deep-water regions builds up approximately one month later than that occurs in
545 the nearshore areas. This is consistent with the conclusion from Wang et al (2019) by
546 comparing the in-situ water temperature records at two stations located at the main
547 basin and the eastern small basin, respectively.

548 According to the POM results, the summer thermal stratification is basically
549 established over LNC when the spring thermal bar eventually arrives at the mid-lake

550 area and vanishes around 10th June (not shown). From May to June, the
551 isobath-following temperature pattern still exists but becomes less pronounced as the
552 consequence of the horizontal basin-scale water/energy exchanges, indicating the
553 important effects of gyre-related hydrodynamics on large-lake thermal states. The
554 lake-averaged LST increases from 3.17 °C to 7.7 °C (Figures 10b and d). In contrast to
555 the weak depth-averaged water flow reaching a few cm s⁻¹ in May, the mean lake
556 current in June increases in magnitude and is featured by two organized
557 contour-rotating gyres in geostrophic balance with the density fields (Figure 10d). The
558 density-driven circulation in the central deep regions is cyclonic and the thermocline
559 has a distinctive dome shape, resembling that in the deeper basin of Lake Michigan and
560 Lake Erie (Beletsky and Schwab 2008; Beletsky et al., 2013). The eastern small basin is
561 characterized by an anticyclonic circulation and a bowl-shaped thermocline. The two
562 basin-scale gyres in June still remain the dominant monthly circulation patterns in July
563 despite with some discrepancies (Figure 10f). In July, the circulation speed increases
564 slightly with the developing summer stratification, which can be indicated by the
565 deepening and temperature increase of the main thermocline. The enhanced cyclonic
566 flow in the main basin further generates evident mid-lake upwelling due to the upward
567 Ekman transport, resulting in the thermocline's dome shape. In August, the gyration
568 features of the depth-averaged currents become less pronounced and the strength of
569 mid-lake upwelling gets weaker, failing to maintain the domed thermocline (Figures

570 10g and h). The lake circulation, especially over the top mixed layer, is likely
571 influenced by the surface winds and characterized by a long nearshore flow along the
572 northwestern coastal regions, which significantly modifies the thermal structures in the
573 upper water body (Figure 10g). On one hand, as the warm water is advected following
574 the nearshore currents, the monthly mean LST in August exhibits a northwest
575 increasing trend different from the isobath-following LST pattern in May-July. On the
576 other hand, the prevailing offshore (onshore) currents can produce the upwelling
577 (downwelling) events and thus lead to the upward (downward) curved isotherms
578 around 90.82°E (90.35°E) (Figures 10g and h). Overall, from June to August, the
579 thermal stratification of LNC is in its developing phase and the monthly lake-averaged
580 LST exhibit a stepwise increase from 7.7°C in June to 10.75°C in July and 12.07°C in
581 August.

582 Since September, LNC begins to lose vast net energy and enters the autumnal
583 destratification period due to the decreased net radiations, enhanced over-lake wind,
584 and the large positive lake-air temperature/humidity gradients (Figure 2). From August
585 to September, the lake-averaged LST decreases from 12.07°C to 10.88°C. The
586 depth-averaged currents in September is rather lower with near-zero flow speeds in the
587 central open-water regions (Figure 11b). There exist two weak anticyclonic gyres in the
588 southwestern corner around (30.65°N, 90.5°E) and the eastern small basin, which may

589 be induced by the residual negative current vorticity from previous months. The
590 simultaneous epilimnion shows a slight deepening and the top thermocline possesses
591 bowl shapes across the lake (Figure 11a). Since October, the large-scale 500-hPa wind
592 fields over TP (Maussion et al., 2013) and the local surface winds over LNC both
593 exhibit significant enhancements in their westerly components. As a result, the
594 eastward water currents pick up in speed and transport warm mixolimnion water to the
595 southeastern part of LNC in October. The mixed layer is tilted eastward and the spatial
596 distribution of LST is characterized by a southeast increasing gradient (Figures 11c and
597 d). From September to October, the lake-averaged LST decreases from 10.88°C to
598 8.57°C. In particular, at the end of October, the bowl-shaped mixolimnion at the
599 deep-water Nam Co buoy can deepen to ~30m and the metalimnion is widely
600 distributed across the 30-60m, which supports the remarkable increases (~2°C) of the
601 observed/modeled 31-m, 36-m, and 56-m water temperature during this period (Figures
602 8a and b). Similarly, the wind-induced deepening of mixolimnion/metalimnion would
603 lead to the abrupt increase (~1.5°C) in the 66-m and 83-m water temperature at this
604 station in early November.

605 In November, lake circulation shows a general increase in speed and features a
606 cyclonic flow in the main basin due to the persistent mechanical energy transportation
607 from surface westerlies (Figure 11f). This suggests the common effects of wind forcing

608 and bathymetry on water currents. The lake-averaged LST in November decreases to
609 5.34°C and the thermal stratification greatly weakens (Figure 11e). It is worth noting
610 that the water column in the western coastal regions exhibits a faster destratification
611 speed due to the eastward heat transportation. LNC begins to stratify around 7th
612 November and the whole lake is thermally mixed again on 26th November according to
613 the POM modeled daily evolution of thermal structures. Given that POM gives a
614 postponed prediction in the destratification date at Nam Co buoy (20th November
615 versus observed 7th November), the actual total destratification date for LNC is
616 speculated to be around mid-November. Since then, when the LST gradually
617 decreases to T_{dmax} in December, a typical autumn thermal bar forms in the coastal
618 regions first and moves progressively toward the lake center (Figure 11g), causing the
619 LNC to enter into the overturning period. From POM results, the autumn thermal bar
620 lasts for approximate one month, comparable to the lifetime of spring thermal bar, and
621 eventually vanishes at the mid-lake regions around 26th December. Then the thermal
622 state in LNC is mainly characterized by an inverse and weak wintertime stratification.
623 At the monthly mean timescale, LST in December exhibits a negative
624 nearshore-offshore temperature gradient and the lake-averaged LST decreases to
625 2.64°C (Figure 11h). The wind-induced lake circulation features a pronounced cyclonic
626 vorticity in the main basin, which gives rise to the upward movement of warm
627 hypolimnion and works in concert with the gravitationally-driven convection to

strengthen the top-to-bottom mixing during the overturning period.

4. Summary and Discussion

In this study, with the guidance of both the valuable 1-yr in-situ water temperature records and the satellite observations during May-December 2013, we explored the performances of the 3-D POM and 1-D WRF-Lake in reproducing the thermal structures of LNC, the second largest lake over central TP. Moreover, we also present detailed discussions about the monthly development of 3-D lake thermodynamics and related circulation patterns based on POM simulations. Main findings are summarized as follows:

Both models can well reproduce the daily evolution of the observed $TLake_{3m}$ at the deep-water buoy (~93m) in LNC, with the TC/TS exceeding 0.95. In terms of the magnitude, WRF-Lake tends to underestimate $TLake_{3m}$, especially during fall-winter periods (September-December). However, POM exhibits preferable capabilities in reproducing the rapid $TLake_{3m}$ increase since June, the gradual $TLake_{3m}$ decrease during destratification/overturning period, and the transient $TLake_{3m}$ oscillating events around mid-December, suggesting that the hydrodynamic POM is more reasonable in capturing the seasonal and synoptic response processes of lake temperature to the regional atmospheric conditions. The BIAS (RMSE) of the modeled $TLake_{3m}$ during May-December is improved from -1.05°C (1.26°C) in WRF-Lake to

647 0.2°C (0.52°C) in POM.

648 Meanwhile, POM also performs better than WRF-Lake in reproducing the spatial
649 distribution of bimonthly LST, which emphasized again that the complex
650 temperature-current interactions must be considered for reasonably reproducing the
651 spatial variability of LST over large TP lakes. For example, during the spring-summer
652 warming periods (May-August), LST is mainly characterized by a persistent
653 nearshore-offshore gradient due to the differential heating mechanism (Monismith et
654 al., 1990), where shallower coastal regions with smaller heat capacity warms faster in
655 response to the intensified radiative heating. This cross-isobath temperature gradient
656 could last for several months and tend to transport vast energy to the mid-lake heat
657 deficit regions through both enhanced thermal diffusion and geostrophic balanced
658 water flows (Beletsky and Schwab 2008; Song et al., 2004). However, as the lake
659 thermodynamics in WRF-Lake is simplified as just vertical with no horizontal
660 water/energy exchanges, the modeled LST is featured by excessively warm shorelines
661 and a pronounced central ‘cold pool’ (Figures 3c and f). The modeled lake
662 temperature at the deep-water Nam Co buoy shows inadequate summertime warming
663 strength and the thermal stratification builds up later than the observation (15th June
664 versus the observed 4th June). Additionally, the missing flow-dependent water/energy
665 transport in WRF-Lake leads to smaller mid-lake heat storage during May-August

666 than that in observation or POM simulations, as implied by the metalimnion (16-36m)
667 temperature (Figure 8). The less heat retention simulated by WRF-Lake would further
668 work with its unresolved upward Ekman heat transport to jointly contribute the
669 significant LST underestimation during fall-winter (September-December). At the
670 Nam Co water temperature station, WRF-Lake underestimates the autumnal lake
671 column temperature with a distinct shallower and much colder mixed layer, leading to
672 the earlier destratification (31th October versus 7th November in observation) and the
673 onset of wintertime inverse thermal stratification.

674 Model intercomparison indicates that both the local lake-air feedbacks and the
675 heat redistribution processes related to the lake thermohydrodynamics should be
676 considered for better representing the spatiotemporal variability of LST and the
677 vertical thermal structures. This is also of great necessities for researching the
678 development of important limnological phenomena and their ecological impacts. With
679 the guidance of in-situ water temperature records and previous observation work over
680 LNC, we give a first-step discussion about its monthly 3-D thermal structure and
681 circulations based on POM results. The springtime overturning processes of LNC
682 occur from 1th May to 10th June 2013, during which typical thermal bar form in the
683 coastal region first in response to the density instabilities triggered by penetrating
684 radiative heating, and then moves progressively towards the center LNC. The thermal

685 stratification builds up around early June and develops with deepening
686 mixolimnion/thermocline during summer (June-August), with the lake-averaged LST
687 increases from 7.7°C to 12.07°C. In terms of the summer lake circulation, the
688 depth-averaged currents in the main basin (eastern small basin) exhibits a cyclonic
689 (anticyclonic) gyre in geostrophic equilibrium with the density fields. The
690 thermocline in the eastern small basin possesses a bowl shape throughout summer,
691 while the top thermocline in the main basin features dome shapes in June-July and
692 bowl shape in August because the epilimnetic water flow experiences a
693 transformation from cyclonic gyre to pronounced long nearshore currents. Since
694 September, LNC enters the autumnal destratification period and is speculated to be
695 thermally mixed again around mid-November due to the decreased solar radiation and
696 significant surface net heat flux loss. With the LST further decreases to T_{dmax}, the
697 autumnal thermal bar develops in the western part of LNC first and gradually turns
698 over the whole water body until the wintertime inverse thermal stratification basically
699 builds up around mid-December. The lake circulation during October-December is
700 characterized by eastward water flow or a dominant cyclonic gyre in the main basin,
701 which can be attributed to the interplay between prevailing surface westerlies and lake
702 bathymetry.

703 At present, there still exist some aspects to be improved for expanding POM's

704 applicability in researching the lake thermal evolution of LNC or other large deep lakes
705 over TP. First, for the deep-water Nam Co buoy, the modeled mixed layer depth is
706 shallower and the destratification date is delayed about two weeks, implying that the
707 vertical mixing strength is underestimated due to the lacking of nonbreaking
708 wave-induced mixing in current POM. Possible remedies are to implement the MY-2.5
709 turbulence closure scheme with a wind-wave-induced parameterization (Hu and Wang
710 [2010](#); Bai et al., [2013](#)) or to couple with a surface wave model, i.e. WAVEWATCH III
711 (Tolman [2009](#)). Additionally, as most TP lakes possess long-lasting ice-covered periods
712 due to their high-altitude features, it is of great necessity to incorporate an ice
713 component into POM in the future. This is especially important for the ice
714 formation/melting periods when the lake thermohydrodynamics are influenced by both
715 the ice movement and its modifications on lake surface layer properties (i.e. albedo,
716 thermal conductivity, and water salinity).

717 **Acknowledgement.** This study is supported by National Natural Science Foundation of China
718 under Grants 41975081, the National Key R&D Program of China under Grant 2017YFA0604301,
719 the Jiangsu University “Blue Project” outstanding young teachers training object, and the
720 Fundamental Research Funds for the Central Universities and the Jiangsu Collaborative Innovation
721 Center for Climate Change. We are grateful to NASA for providing the MODIS LST product
722 (MOD11; available at <https://modis.gsfc.nasa.gov/data/dataproduct/mod11.php>) and the Institute of

723 Tibetan Plateau Research, Chinese Academy of Sciences (ITPCAS) for providing the China
724 Meteorological Forcing Dataset (CMFD) (available at <http://en.tpedatabase.cn/portal>). We also
725 appreciate Dr. Junbo Wang and Dr. Lei Huang for providing the station data, which is available at
726 the website <http://en.tpedatabase.cn/portal/MetaDataInfo.jsp?MetaDataId=177>.

727 **Reference**

- 728 Aijaz, S., M Ghantous, AV Babanin, I Ginis, B Thomas and G Wake (2017). Nonbreaking
729 wave-induced mixing in upper ocean during tropical cyclones using coupled
730 hurricane-ocean-wave modeling. *J. Geophys. Res. Oceans*, 122, 3939-3963. Doi:
731 [10.1002/2016JC012219](https://doi.org/10.1002/2016JC012219)
- 732 Ao, YH, SH Lyu and ZG Li (2018). Numerical simulation of the climate effect of high-altitude
733 lakes on the Tibetan Plateau. *Sciences in Cold and Arid Regions*, 10(5): 0379-0391. Doi:
734 [10.3724/SP.J.1226.2018.00379](https://doi.org/10.3724/SP.J.1226.2018.00379)
- 735 Bai, XZ., J Wang, DJ Schwab, Y Yang, L Luo, GA Leshkevich and SZ Liu (2013). Modeling
736 1993-2008 climatology of seasonal general circulation and thermal structure in the Great
737 Lakes using FVCOM. *Ocean Modelling*, 65: 40-63. Doi: [10.1016/j.ocemod.2013.02.003](https://doi.org/10.1016/j.ocemod.2013.02.003)
- 738 Beletsky, D. and DJ Schwab (2001). Modelling circulation and thermal structures in Lake
739 Michigan: Annual cycle and interannual variability. *J. Geophys. Res.*, 106: 745-771. Doi:
740 [10.1029/2000JC000691](https://doi.org/10.1029/2000JC000691)
- 741 —, JD Schwab and M McCormick (2006). Modeling the 1998-2003 summer circulation and
742 thermal structure in Lake Michigan. *J. Geophys. Res.* 111, C10010. Doi:
743 [10.1029/2005JC003222](https://doi.org/10.1029/2005JC003222)
- 744 — and JD Schwab (2008). Climatological circulation in Lake Michigan. *Geophys. Res. Lett.*,

745 35, L21604. [Doi: 10.1029/2008GL035773](https://doi.org/10.1029/2008GL035773)

746 —, N Hawley, YR Rao, HA Vanderploeg, R Beletsky, DJ Schwab and SA Ruberg (2012).
747 Summer thermal structure and anticyclonic circulation of Lake Erie. *Geophys. Res. Lett.*, 39,
748 L06605. [Doi: 10.1029/2012GL051002](https://doi.org/10.1029/2012GL051002)

749 —, N Hawley and YR Rao (2013). Modeling summer circulation and thermal structure of Lake
750 Erie. *J. Geophys. Res.*, 118, 6238-6252. [Doi: 10.1002/2013JC008854](https://doi.org/10.1002/2013JC008854)

751 Bennington, V., GA McKinley, N Kimura and CH Wu (2010). General circulation of Lake Superior:
752 Mean, variability, and trends from 1979 to 2006. *J. Geophys. Res.*, 115, C12015. [Doi: 10.1029/2010JC006261](https://doi.org/10.1029/2010JC006261)

753 [10.1029/2010JC006261](https://doi.org/10.1029/2010JC006261)

754 —, M Notaro and KD Holman (2014). Improving climate sensitivity of deep lakes within a
755 regional climate model and its impact on simulated climate. *J. Clim.*, 27: 2886-2911. [Doi: 10.1175/JCLI-D-13-00110.1](https://doi.org/10.1175/JCLI-D-13-00110.1)

756 [10.1175/JCLI-D-13-00110.1](https://doi.org/10.1175/JCLI-D-13-00110.1)

757 Biermann, T., W Babel, WQ Ma, XL Chen, E Thiem, YM Ma, and T Foken (2014). Turbulent flux
758 observations and modelling over a shallow lake and a wet grassland in the Nam Co basin,
759 Tibetan Plateau. *Theor. Appl. Climatol.*, 116, 301–316. [Doi: 10.1007/s00704-013-0953-6](https://doi.org/10.1007/s00704-013-0953-6)

760 Blumberg, AF and GL Mellor (1987). A description of a three-dimensional coastal ocean
761 circulation model, three-dimensional coastal ocean circulation model. *Three-Dimensional*
762 *Ocean Models*, American Geophysical Union, Washington DC, Chapter 4. [Doi: 10.1029/CO004p0001](https://doi.org/10.1029/CO004p0001)

763 [10.1029/CO004p0001](https://doi.org/10.1029/CO004p0001)

764 Blokhina NS and DI Selin (2019). Spring thermal bar formation in a water reservoir with a
765 complex bottom relief (for Lake Ladoga as an example). *Moscow University Physics*
766 *Bulletin*, 74(1):58-63. [Doi: 10.3103/S0027134919010065](https://doi.org/10.3103/S0027134919010065)

767 Chen, YY., K Yang, J He, J Qin, J Shi, J Du and Q He (2011). Improving land surface temperature

768 modeling for dry land of China. *J. Geophys. Res.*, 116, D20104. [Doi: 10.1029/2011JD015921](https://doi.org/10.1029/2011JD015921)

769 Copernicus Climate Change Service (C3S) (2019). C3S ERA5_Land reanalysis. Copernicus
 770 Climate Change Service. [Doi: 10.24381/cds.e2161bac](https://doi.org/10.24381/cds.e2161bac)

771 Cui, LB and XY Li (2014). Characteristics of stable isotope and hydrochemistry of the
 772 groundwater around Qinghai Lake, NE Qinghai-Tibet Plateau, China. *Environ. Earth. Sci.*, 71:
 773 1159-1167. [Doi: 10.1007/s12665-013-2520-y](https://doi.org/10.1007/s12665-013-2520-y)

774 Dai, YF., L Wang, TD Yao, XY Li, LJ Zhu, and XW Zhang (2018a). Observed and Simulated
 775 Lake Effect Precipitation Over the Tibetan Plateau: An Initial Study at Nam Co Lake. *J.*
 776 *Geophys. Res. Atmos.*, 123, 6746–6759. [Doi:10.1029/2018JD028330](https://doi.org/10.1029/2018JD028330)

777 Dai, YJ., N Wei, AN Huang, SG Zhu, W ShangG, H Yuan, SP Zhang, and SF Liu (2018b). The
 778 Lake Scheme of the Common Land Model and its performance evaluation. *Chinese Science*
 779 *Bulletin* 63(28-29). [Doi:10.1360/N972018-00609](https://doi.org/10.1360/N972018-00609)

780 Garratt JR (1977). Review of drag coefficients over oceans and continent. *Mon. Wea. Rev.*,
 781 105(7):915-929. [Doi:10.1175/1520-0493\(1977\)105<0915:RODCOO>2.0.CO;2](https://doi.org/10.1175/1520-0493(1977)105<0915:RODCOO>2.0.CO;2)

782 Gerken, T., W Babel, FL Sun, M Herzog, YM Ma, T Foken and HF Graf (2013a). Uncertainty in
 783 atmospheric profiles and its impact on modeled convection development at Nam Co Lake,
 784 Tibetan Plateau. *J. Geophys. Res. Atmos.*, 118, 12: 317-331. [Doi: 10.1002/2013JD020647](https://doi.org/10.1002/2013JD020647)

785 —, T Biermann, W Babel, M Herzog, YM Ma, T Foken, and HF Graf (2013b). A modelling
 786 investigation into lake-breeze development and convection triggering in the Nam Co Lake
 787 basin, Tibetan Plateau. *Theor. Appl. Climatol.*, 117(1-2):149-167.
 788 [Doi:10.1007/s00704-013-0987-9](https://doi.org/10.1007/s00704-013-0987-9)

789 Gill A (1982). *Atmosphere-Ocean Dynamics*, Academic, New York.

790 Gou, P., QH Ye, T Che, Q Feng, BH Ding, CG Lin and JB Zong (2017). Lake ice phenology of
791 Nam Co, Central Tibetan Plateau, China, derived from multiple MODIS data products. J.
792 Great Lake Res. [Doi: 10.1016/j.jglr.2017.08.011](https://doi.org/10.1016/j.jglr.2017.08.011)

793 Gu, HP., JM Jin, YH Wu, MB EK, and ZM Subin (2015). Calibration and validation of lake
794 surface temperature simulations with the coupled WRF-lake model. Climatic. Change.,
795 129:471–483. [Doi:10.1007/s10584-013-0978-y](https://doi.org/10.1007/s10584-013-0978-y)

796 Guo, YH., YS Zhang, N Ma, JQ Xu, and T Zhang (2019). Long-term changes in evaporation over
797 Siling Co Lake on the Tibetan Plateau and its impact on recent rapid lake expansion. Atmos.
798 Res., 216, 141-150. [Doi: 10.1016/j.atmosres.2018.10.006](https://doi.org/10.1016/j.atmosres.2018.10.006)

799 Haginoya, S., H Fujii, T Kuwagata, JQ Xu, Y Ishigooka, SC Kang and YJ Zhang (2009). Air-lake
800 interaction features found in heat and water exchanges over Nam Co on the Tibetan Plateau.
801 SOLA 5(1): 172-175. [Doi: 10.2151/sola.2009-044](https://doi.org/10.2151/sola.2009-044)

802 —, H Fuiji, JH Sun and JY Liu (2012). Features of air-lake interaction in heat and water
803 exchanges over Erhai Lake. Journal of the Meteorological Society of Japan, 90C: 55-73. [Doi:
804 10.2151/jmsj.2012-C04](https://doi.org/10.2151/jmsj.2012-C04)

805 He, J., K Yang, WJ Tang, H Lu, J Qin, YY Chen and X Li (2020). Data Descriptor: The first
806 high-resolution meteorological forcing dataset for land process studies over China. Scientific
807 Data, 7(25): 1-11. [Doi: 10.1038/s41597-020-0369-y](https://doi.org/10.1038/s41597-020-0369-y)

808 Hostetler, SW., GT Bates, and F Giorgi (1993). Interactive coupling of a lake thermal model with
809 a regional climate model. J. Geophys. Res., 98:5045–5057. [Doi: 10.1029/92JD02843](https://doi.org/10.1029/92JD02843)

810 Hook, SJ., FJ Prata, RE Alley, A Abtahi, RC Richards, SG Schladow and SO Palmarsson (2003).
811 Retrieval of lake bulk and skin temperature using Along-Track Scanning Radiometer
812 (ATSR-2) data: a case study using Lake Tahoe, California. Journal of Atmospheric and

813 Oceanic Technology 20(4):534-548. Doi:
814 [10.1175/1520-0426\(2003\)20<534:ROLBAS>2.0.CO;2](https://doi.org/10.1175/1520-0426(2003)20<534:ROLBAS>2.0.CO;2)

815 Hu, HG and J Wang (2010). Modeling effects of tidal and wave mixing on circulation and
816 thermohaline structures in the Bering Sea: Process studies. J. Geophys. Res., 115, C01006.
817 Doi: [10.1029/2008JC005175](https://doi.org/10.1029/2008JC005175)

818 Huang, AN., YR Rao, and YY Lu (2010). Evaluation of a 3-D hydrodynamic model and
819 atmospheric forecast forcing using observations in Lake Ontario. J. Geophys. Res., 115,
820 C02004. Doi:[10.1029/2009JC005601](https://doi.org/10.1029/2009JC005601)

821 —, Lazhu, JB Wang, YJ Dai, K Yang, N Wei, LJ Wen, Y Wu, XY Zhu, XD Zhang, SX Cai
822 (2019). Evaluating and Improving the Performance of Three 1-D Lake Models in a Large
823 Deep Lake of the Central Tibetan Plateau. J. Geophys. Res., Doi: [10.1029/2018JD029610](https://doi.org/10.1029/2018JD029610)

824 Huang, CJ and FL Qiao (2010). Wave-turbulence interaction and its induced mixing in the upper
825 ocean. J. Geophys. Res., 115, C04026. Doi: [10.1029/2009JC005853](https://doi.org/10.1029/2009JC005853)

826 Huang, L., JB Wang, LP Zhu, JT Ju, and G Daut (2017). The Warming of Large Lakes on the
827 Tibetan Plateau: Evidence From a Lake Model Simulation of Nam Co, China, During 1979–
828 2012. J. Geophys. Res., 122, 13,095–13,107. Doi: [10.1002/2017JD027379](https://doi.org/10.1002/2017JD027379)

829 Kantha, LH. And CA Clayson (2004). On the effect of surface gravity waves on mixing in the
830 oceanic mixing layer. Ocean Modelling, 6(2): 101-124. Doi:
831 [10.1016/S1463-5003\(02\)00062-8](https://doi.org/10.1016/S1463-5003(02)00062-8)

832 Ke, LH and CQ Song (2014). Remotely sensed surface temperature variation of an inland saline
833 lake over the central Qinghai-Tibet Plateau. ISPRS Journal of Photogrammetry and Remote
834 Sensing, 98: 157-167. Doi: [10.1016/j.isprsjprs.2014.09.007](https://doi.org/10.1016/j.isprsjprs.2014.09.007)

835 Kirillin, G., LJ Wen and T Shatwell (2017). Seasonal thermal regime and climatic trends in lakes

836 of the Tibetan highlands. *Hydrol. Earth Syst. Sci.*, 21, 1895-1909. [Doi: 10.5194/hess-21-1895-2017](https://doi.org/10.5194/hess-21-1895-2017)

837

838 Lazhu, K Yang, JB Wang, YB Lei, YY Chen, LP Zhu, BH Ding, and J Qin (2016). Quantifying

839 evaporation and its decadal change for Lake Nam Co, central Tibetan Plateau. *J. Geophys.*

840 *Res.*, 121, 7578-7591. [Doi:10.1002/2015JD024523](https://doi.org/10.1002/2015JD024523)

841 Leon, LF., DCL Lam, WM Schertzer, DA Swayne and J Imberger (2007). Towards coupling a 3D

842 hydrodynamic lake model with the Canadian Regional Climate Model: Simulation on Great

843 Slave Lake. *Environmental Modelling & Software* 22, 787-796. [Doi: 10.1016/j.envsoft.2006.03.005](https://doi.org/10.1016/j.envsoft.2006.03.005)

844

845 Lei, YB., K Yang, B Wang, YW Sheng, B W.Bird, GQ Zhang and Ld Tian (2014). Response of

846 inland lake dynamics over the Tibetan Plateau to climate change. *Climatic Change*, 125:

847 281-290. [Doi: 10.1007/s10584-014-1175-3](https://doi.org/10.1007/s10584-014-1175-3)

848 Li, ZG., SH Lv, YH Ao, LJ Wen, L Zhao, and SY Wang (2015) Long-term energy flux and

849 radiation balance observations over Lake Ngoring, Tibetan Plateau. *Atmospheric Research*

850 155:13-25. [Doi: 10.1016/j.atmosres.2014.11.019](https://doi.org/10.1016/j.atmosres.2014.11.019)

851 ———, YH Ao, SH Lv, JH Lang, LJ Wen, V Stepanenko, XH Meng, and L Zhao (2018).

852 Investigation of the ice surface albedo in the Tibetan Plateau lakes based on the field

853 observation and MODIS products. *Journal of Glaciology*, 1-11. [Doi: 10.1017/jog.2018.35](https://doi.org/10.1017/jog.2018.35)

854 Liu, HZ., JW Feng, JH Sun, L Wang and AL Xu (2015). Eddy covariance measurements of water

855 vapor and CO₂ fluxes above the Erhai Lake. *Science China: Earth Sciences*, 58: 317-328.

856 [Doi: 10.1007/s11430-014-4828-1](https://doi.org/10.1007/s11430-014-4828-1)

857 Long, Z., W Perrie, J Gyakum, R Laprise and D Caya (2007). Northern lake impacts on local

858 season climate. *Journal of Hydrometeorology*, 8(4): 881-896. [Doi: 10.1175/JHM591.1](https://doi.org/10.1175/JHM591.1)

859 Lu, SL., J Ma, XQ Ma, HL Tang, HL Zhao and MHA Baig (2019). Time series of the inland
 860 surface water dataset in China (ISWDC) for 2000-2016 derived from MODIS archives. Earth
 861 Syst. Sci. Data, 11: 1099-1108. [Doi: 10.5149/essd-11-1099-2019](https://doi.org/10.5149/essd-11-1099-2019)

862 Ma, RH., GS Yang, HT Duan, JH Jiang, SM Wang, XZ Feng, AN Li, FX Kong, B Xue, JL Wu and
 863 SJ Lin (2011). China's lakes at present: Number, area and spatial distribution. Sci. China
 864 Earth Sci, 54: 283-289. [Doi: 10.1007/s11430-010-4052-6](https://doi.org/10.1007/s11430-010-4052-6)

865 Martynov, A., L Sushama and R Laprise (2010). Simulation of temperature freezing lakes by
 866 one-dimensional lake models: performance assessment for interactive coupling with regional
 867 climate models. Boreal Environment Research 15, 143-164.

868 Maussion, F., D Scherer, T Molg, E Collier, J Curio, and R Finkelburg (2013). Precipitation
 869 seasonality and variability over the Tibetan Plateau as Resolved by the High Asia Reanalysis.
 870 J. Clim., 1910-1927. [Doi: 10.1175/JCLI-D-13-00282.1](https://doi.org/10.1175/JCLI-D-13-00282.1)

871 Mellor, GL and T Yamada (1982). Developmen of a turbulence closure model for geophysical
 872 fluid problems. Reviews of Geophysics and Space Physics, 20(4): 851-875. [Doi: 10.1029/RG020i004p00851](https://doi.org/10.1029/RG020i004p00851)

874 Mironov DV (2008). Parameterization of lakes in numerical weather prediction. Description of a
 875 lake model [R]. COSMO technical report. Deutscher Wetterdienst, Offenbach am Main,
 876 Germany.

877 Monismith, SG., J Imberger and ML Morison (1990). Convective motions in the sidearm of a
 878 small reservoir. Limnol. Oceanogr., 35(8): 1676-1702.

879 Murakami, T., H Terai, Y Yoshiyama, T Tezuka, LP Zhu, T Matsunaka and M Nishimura (2007).
 880 The second investigation of Lake Puma Yum Co located in the Southern Tibetan Plateau,
 881 China. Limnology, 8:331-335. [Doi:10.1007/s10201-007-0208-2](https://doi.org/10.1007/s10201-007-0208-2)

882 Notaro, M., A Zarrin, S Vavrus and V. Bennington (2013). Simulation of heavy lake-effect
883 snowstorms across the Great Lakes basin by RegCM4: Synoptic climatology and variability.
884 Mon. Wea. Rev., 141, 1990–2014. [Doi:10.1175/MWR-D-11-00369.1](https://doi.org/10.1175/MWR-D-11-00369.1)

885 Nyamweya, C., C Desjardins, S Sigurdsson, T Tomasson, A Taabu-munyaho, L Sitoki and G
886 Stefansson (2016). Simulation of Lake Victoria circulation patterns using the Regional Ocean
887 Modelling System (ROMS). PLoS ONE 11(3): e0151272. [Doi: 10.1371/journal.pone.0151272](https://doi.org/10.1371/journal.pone.0151272)

889 Qi, MM., XJ Yao, XF Li, HY Duan, YP Gao, and J Liu (2019). Spatiotemporal characteristics of
890 Qinghai Lake ice phenology between 2000 and 2016. J. Geogr. Sci. 2019, 29(1): 115-130.
891 [Doi: 10.1007/s11442-019-1587-0](https://doi.org/10.1007/s11442-019-1587-0)

892 Rao, YR., MG Skafel and MN Charlton (2004). Circulation and turbulent exchange characteristics
893 during the thermal bar in Lake Ontario. Limnol. Oceanogr., 49(6): 2190-2200. [Doi: 10.4319/lo.2004.49.6.2190](https://doi.org/10.4319/lo.2004.49.6.2190)

895 Rao, YR and DJ Schwab (2007). Transport and mixing between the coastal and offshore waters in
896 the Great Lakes: a review. J. Great Lakes Res., 33:202-218.
897 [Doi:10.3394/0380-1330\(2007\)33\[202:TAMBTC\]2.0.CO;2](https://doi.org/10.3394/0380-1330(2007)33[202:TAMBTC]2.0.CO;2)

898 Schwab, DJ and D Beletsky (2003). Relative effects of wind stress curl, topography, and
899 stratification on large-scale circulation in Lake Michigan. J. Geophys. Res. 108, 3044. [Doi: 10.1029/2001JC001066](https://doi.org/10.1029/2001JC001066)

901 Sharma, A., AF Hamlet, HJS Fernando, CE Catlett, DE Horton, VR Kotamarthi, DAR Kristovich,
902 AI Packman, JL Tank, and DJ Wuebbles (2018). The Need for an Integrated

903 Land-Lake-Atmosphere Modeling System, Exemplified by North America's Great Lakes
 904 Region. *Earth's Future*, 6, 1366–1379. [Doi:10.1029/2018EF000870](https://doi.org/10.1029/2018EF000870)

905 Shepard D (1968). A two-dimensional interpolation function for irregularly-spaced data.
 906 Proceedings of the 1968 ACM national conference, 27-29 August 1968, New York, pp
 907 517-524. [Doi: 10.1145/800186.810616](https://doi.org/10.1145/800186.810616)

908 Song, CQ., B Huang, and LH Ke (2014). Inter-annual changes of alpine inland lake water storage
 909 on the Tibetan Plateau, detection and analysis by integrating satellite altimetry and optical
 910 imagery. *Hydrological Processes* 28(4), 2411-2418. [Doi:10.1002/hyp.9798](https://doi.org/10.1002/hyp.9798)

911 Song, KS., M Wang, J Du, Y Yuan, JH Ma, GY Mu (2016). Spatiotemporal Variations of Lake
 912 Surface Temperature across the Tibetan Plateau Using MODIS LST Product. *Remote Sens.*, 8,
 913 854. [Doi:10.3390/rs8100854](https://doi.org/10.3390/rs8100854)

914 Su, DS., XQ Hu, LJ Wen, SH Lyu, XQ Gao, L Zhao, ZG Li, J Du, and G Kirillin (2019). Numerical
 915 study on the response of the largest lake in China to climate change. *Hydrol. Earth. Syst. Sci.*,
 916 23, 2093-2109. [Doi: 10.5194/hess-23-2093-2019](https://doi.org/10.5194/hess-23-2093-2019)

917 Subin, ZM., WJ Riley, and D Mironov (2012). An improved lake model for climate simulations:
 918 Model structure, evaluation, and sensitivity analyses in CESM1. *J. Adv. Model. Earth. Syst.*,
 919 4, M02001. [Doi: 10.1029/2011MS000072](https://doi.org/10.1029/2011MS000072)

920 Titzel, DJ and JA Austin (2014). Winter thermal structure of Lake Superior. *Limnol. Oceanogr.*,
 921 1336-1348. [Doi: 10.4319/lo.2014.59.4.1336](https://doi.org/10.4319/lo.2014.59.4.1336)

922 Tolman HL (2009). User manual and system documentation of WAVEWATCH III version 3.14.
 923 Tech. Note 276, NOAA/NWS/NCEP/EMC/MMAB, Camp Springs, Md

-
- 924 Tsydenov BO (2019). A numerical study of the thermal bar in shallow water during the autumn
925 cooling. *Journal of Great Lakes Research*, 45:715-725. [Doi: 10.1016/j.jglr.2019.05.012](https://doi.org/10.1016/j.jglr.2019.05.012)
- 926 Verburg, P and JP Antenucci (2010). Persistent unstable atmospheric boundary layer enhances
927 sensible and latent heat loss in a tropical great lake: Lake Tanganyika. *J. Geophys. Res.*, 115,
928 D11109. [Doi: 10.1029/2009JD012839](https://doi.org/10.1029/2009JD012839)
- 929 Wan, W., PF Xiao, XZ Feng, H Li, RH Ma, HT Duan and LM Zhao (2014). Monitoring lake
930 changes of Qinghai-Tibetan Plateau over the past 30 years using satellite remote sensing data.
931 *Chin. Sci. Bull.*, 59. [Doi: 10.1007/s11434-014-0128-6](https://doi.org/10.1007/s11434-014-0128-6)
- 932 Wan, Z., Y Zhang, Q Zhang, and ZL Li (2004). Quality assessment and validation of the MODIS
933 global land surface temperature, *Int. J. Remote Sens.*, 25, 261–274,
934 [Doi:10.1080/0143116031000116417](https://doi.org/10.1080/0143116031000116417)
- 935 Wang, BB., YM Ma, XL Chen, WQ Ma, ZB Su, and M Menenti (2015). Observation and
936 simulation of lake-air heat and water transfer processes in a high-altitude shallow lake on the
937 Tibetan Plateau. *J. Geophys. Res. Atmos.*, 120,12,327–12,344. [Doi: 10.1002/2015JD023863](https://doi.org/10.1002/2015JD023863).
- 938 —, YM Ma, WQ Ma, and ZB Su (2017a) Physical controls on half-hourly, daily, and monthly
939 turbulent flux and energy budget over a high-altitude small lake on the Tibetan Plateau. *J.*
940 *Geophys. Res.*, 122:2289-2303. [Doi:10.1002/2016JD026109](https://doi.org/10.1002/2016JD026109)
- 941 Wang, FS., GH Ni, WJ Riley, JY Tang, DJ Zhu and T Sun (2019). Evaluation of the WRF lake
942 module (v1.0) and its improvements at a deep reservoir. *Geosci. Model Dev.*,
943 12(5):2119-2138. [Doi: 10.5194/gmd-2018-168](https://doi.org/10.5194/gmd-2018-168)
- 944 Wang, JB., LP Zhu, G Daut, JT Ju, X Lin, Y Wang, and XL Zhen (2009) Investigation of
945 bathymetry and water quality of Lake Nam Co, the largest lake on the central Tibetan Plateau.

946 Limnology, 10,149-158. [Doi:10.1007/s10201-009-0266-8](https://doi.org/10.1007/s10201-009-0266-8)

947 —, P Peng, QF Ma and LP Zhu (2010). Modern limnological features of Tangra Yumco and
 948 Zhari Namco Tibetan Plateau. *Journal of Lake Sciences*, 22(4): 629-632

949 —, L Huang, JT Ju, G Daut, Y Wang, QF Ma, LP Zhu, T Haberzettl, J Baade, and R
 950 Mausbacher (2019). Spatial and temporal variations in water temperature in a high-altitude
 951 deep dimictic mountain lake (Nam Co), central Tibetan Plateau. *Journal of Great Lakes*
 952 *Research*. [Doi: 10.1016/j.jglr.2018.12.005](https://doi.org/10.1016/j.jglr.2018.12.005)

953 —, L Huang, JT Ju, ..., and BE Laval (2020). Seasonal stratification of a deep, high-altitude,
 954 dimictic lake: Nam Co, Tibetan Plateau. *Journal of Hydrology*. [Doi: 10.1016/j.jhydrol.2020.124668](https://doi.org/10.1016/j.jhydrol.2020.124668)

955

956 Wang, MD., JZ Hou and YB Lei (2014). Classification of Tibetan lakes based on variations in
 957 seasonal lake water temperature. *Chin. Sci. Bull.*, 59: 4847-4855. [Doi: 10.1007/s11434-014-0588-8](https://doi.org/10.1007/s11434-014-0588-8)

958

959 Wang, XJ., GJ Pang and MX Yang (2017b). Review Precipitation over the Tibetan during recent
 960 decades: a review based on observations and simulations. *Int. J. Climatol.* [Doi: 10.1002/joc.5246](https://doi.org/10.1002/joc.5246)

961

962 Wen, LJ., SH Lv, ZG Li, L Zhao, and N Nagabhatla (2015). Impact of two biggest lakes on local
 963 temperature and precipitation in the Yellow River source region of the Tibetan Plateau.
 964 *Advances in Meteorology*. [Doi:10.1155/2015/248031](https://doi.org/10.1155/2015/248031)

965 —, SH Lv, G Kirillin, ZG Li, and L Zhao (2016). Air–lake boundary layer and performance of a
 966 simple lake parameterization scheme over the Tibetan highlands. *Tellus A: Dynamic*
 967 *Meteorology and Oceanography*, 68:1, 31091. [Doi: 10.3402/tellusa.v68.31091](https://doi.org/10.3402/tellusa.v68.31091)

-
- 968 Wetzel, RG and GE Likens (2000). The heat budget of lakes. In: Limnological Analyses. Springer,
969 New York, NY. [Doi: 10.1007/978-1-4757-3250-4_4](https://doi.org/10.1007/978-1-4757-3250-4_4)
- 970 Wu, Y., AN Huang, B Yang, GT Dong, LJ Wen, Lazhu, ZQ Zhang, ZP Fu, XY Zhu, XD Zhang,
971 and SX Cai (2019). Numerical study on the climatic effect of the lake clusters over Tibetan
972 Plateau in summer. *Clim. Dyn.*, [Doi:10.1007/s00382-019-04856-4](https://doi.org/10.1007/s00382-019-04856-4)
- 973 Xiao, CL., BM Lofgren, J Wang, and PY Chu (2016). Improving the lake scheme within a coupled
974 WRF-lake model in the Laurentian Great Lakes. *J. Adv. Model. Earth. Syst.*, 8, 1969–1985.
975 [Doi:10.1002/2016MS000717](https://doi.org/10.1002/2016MS000717)
- 976 Xiao, F, L Ling, Y Du, Q Feng, Y Yan and H Chen (2013). Evaluation of spatial-temporal
977 dynamics in surface water temperature of Qinghai Lake from 2001 to 2010 by using MODIS
978 data. *J. Arid Land*, 5(4): 452-464. [Doi: 10.1007/s40333-013-0188-5](https://doi.org/10.1007/s40333-013-0188-5)
- 979 Xu, LJ, HZ Liu, Q Du, and L Wang (2016). Evaluation of the WRF-lake model over a highland
980 freshwater in southwest China. *J. Geophys. Res.*, 121. [Doi: 10.1002/2016JD025396](https://doi.org/10.1002/2016JD025396)
- 981 —, HZ Liu, Q Du, L Wang, L Yang, and JH Sun (2018). Differences of atmospheric boundary
982 layer characteristics between pre-monsoon and monsoon period over the Erhai Lake. *Theor.*
983 *Appl. Climatol.*, 135: 305. [Doi:10.1007/s00704-018-2386-8](https://doi.org/10.1007/s00704-018-2386-8)
- 984 Xu, YW., SC Kang, YL Zhang and YJ Zhang (2011). A method for estimating the contribution of
985 evaporative vapor from Nam Co to local atmospheric vapor based on stable isotopes of water
986 bodies. *Chin. Sci. Bull.*, 56: 1511-1517. [Doi: 10.1007/s11434-011-4467-2](https://doi.org/10.1007/s11434-011-4467-2)
- 987 Xue, PF, DJ Schwad and S Hu (2015). An investigation of the thermal response to meteorological
988 forcing in a hydrodynamic model of Lake Superior. *J. Geophys. Res. Oceans*, 120:
989 5233-5253. [Doi: 10.1002/2015JC010740](https://doi.org/10.1002/2015JC010740)
- 990 —, JS Pal, XY Ye, JD Lenters, CF Huang, and PY Chu (2016). Improving the Simulation of

-
- 991 Large Lakes in Regional Climate Modeling: Two-Way Lake–Atmosphere Coupling with a
992 3D Hydrodynamic Model of the Great Lakes. *J. Clim.*, 1605-1627.
993 [Doi:10.1175/JCLI-D-16-0225.1](https://doi.org/10.1175/JCLI-D-16-0225.1)
- 994 Yan, FQ., M Sillanpaa, SC Kang, KS Aho, B Qu, D Wei, XF Li, CL Li, and P A.Raymond (2018).
995 Lakes on the Tibetan Plateau as conduits of greenhouse gases to the atmosphere. *J. Geophys.*
996 *Res.*, 123. [Doi: 10.1029/2017/JG004379](https://doi.org/10.1029/2017/JG004379)
- 997 Yang, XY., YQ Lv, YM Ma and J Wen (2015) Summertime thermally-induced circulations over
998 the Lake Nam Co region of the Tibetan Plateau. *J. Meteorol. Res.*, 29, 305-314. [Doi:](https://doi.org/10.1007/s13351-015-0424-z)
999 [10.1007/s13351-015-0424-z](https://doi.org/10.1007/s13351-015-0424-z)
- 1000 Zhang, GQ., TD Yao, SL Piao, T Bolch, HJ Xie, DL Chen, YH Gao, CM O'Reilly, CK Shum, K
1001 Yang, Y Shuang, YB Lei, WC Wang, Y He, K Shang, XK Yang, and HB Zhang (2017).
1002 Extensive and drastically different alpine lake changes on Asia's high plateaus during the past
1003 four decades. *Geophys. Res. Lett.*, 44, 252–260. [Doi:10.1002/2016GL072033](https://doi.org/10.1002/2016GL072033)
- 1004 — (2018). Changes in lakes on the Tibetan Plateau observed from satellite data and their
1005 responses to climate variations [J]. *Progress in Geography*, 37(2): 214-223. [Doi:](https://doi.org/10.18306/dlkxyj.2018.02.004)
1006 [10.18306/dlkxyj.2018.02.004](https://doi.org/10.18306/dlkxyj.2018.02.004)
- 1007 Zhang, X., KQ Duan, PH Shi, and JH Yang (2016). Effect of lake surface temperature on the
1008 summer precipitation over the Tibetan Plateau. *J. Mt. Sci.*, 13(5):802-810.
1009 [Doi:10.1007/s11629-015-3743-z](https://doi.org/10.1007/s11629-015-3743-z)
- 1010 Zhang, QH., JM Jin, LJ Zhu and SL Lu (2018). Modelling of water surface temperature of three
1011 lakes on the Tibetan Plateau using a physically based lake model. *Atmosphere Ocean*, 2018,
1012 1-7. [Doi: 10.1080/07055900.2018.1474084](https://doi.org/10.1080/07055900.2018.1474084)
- 1013 Zhu, LJ, JM Jin, X Liu, L Tian, and QH Zhang (2017). Simulations of the impact of lakes on local

1014 and regional climate over the Tibetan Plateau. Atmosphere Ocean 1-10.

1015 [Doi:10.1080/07055900.2017.1401—524](https://doi.org/10.1080/07055900.2017.1401524)

1016 **Table 1.** The bimonthly lake-averaged lake surface temperature (LST, unit: °C) from
 1017 MODIS observation and POM/WRF-Lake simulation. The root mean square error
 1018 (RMSE, unit: °C) between the simulation and observation is also presented.

	May-Jun		Jul-Aug		Sep-Oct		Nov-Dec	
	LST	RMSE	LST	RMSE	LST	RMSE	LST	RMSE
MODIS	5.74	—	10.74	—	9.38	—	3.69	—
POM	6.02	1.85	11.57	1.15	9.85	0.66	4.12	0.96
WRF-Lake	6.04	1.78	11.01	0.93	8.20	1.30	1.09	3.05

1019

1020

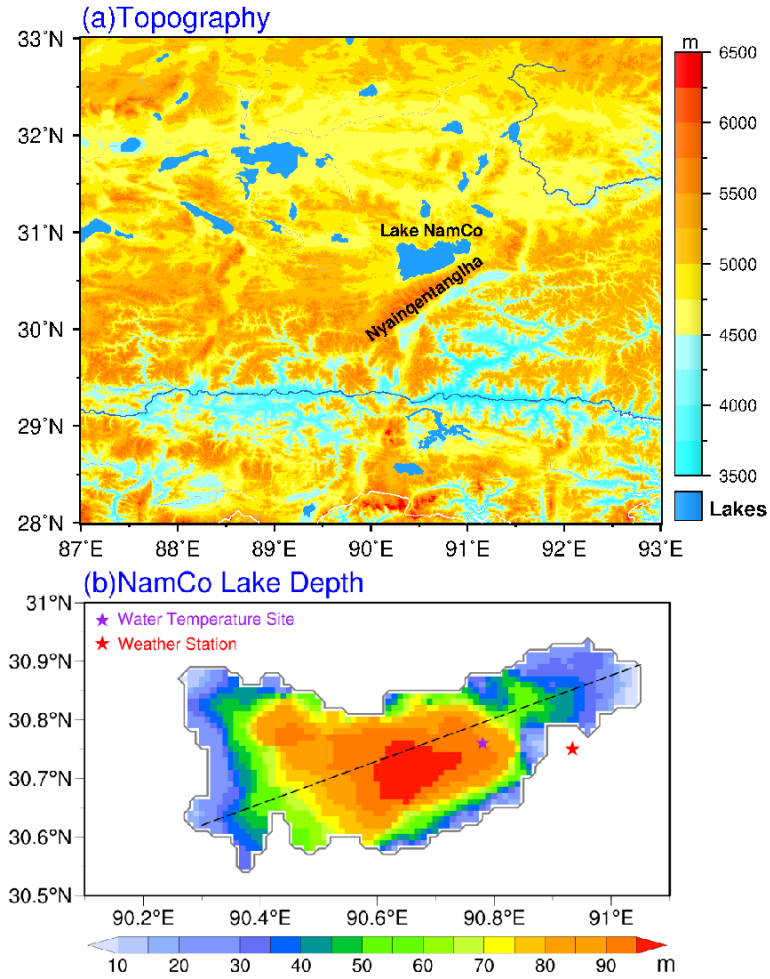
1021

1022

1023

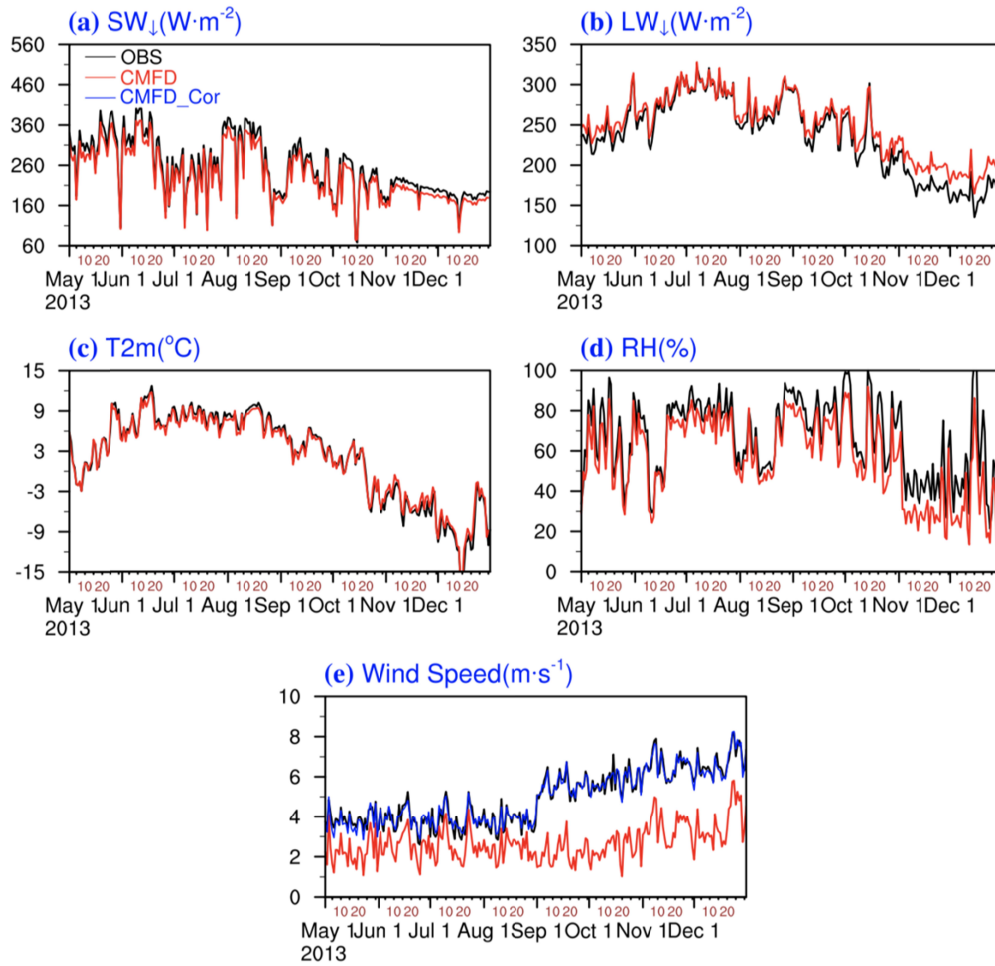
1024

1025



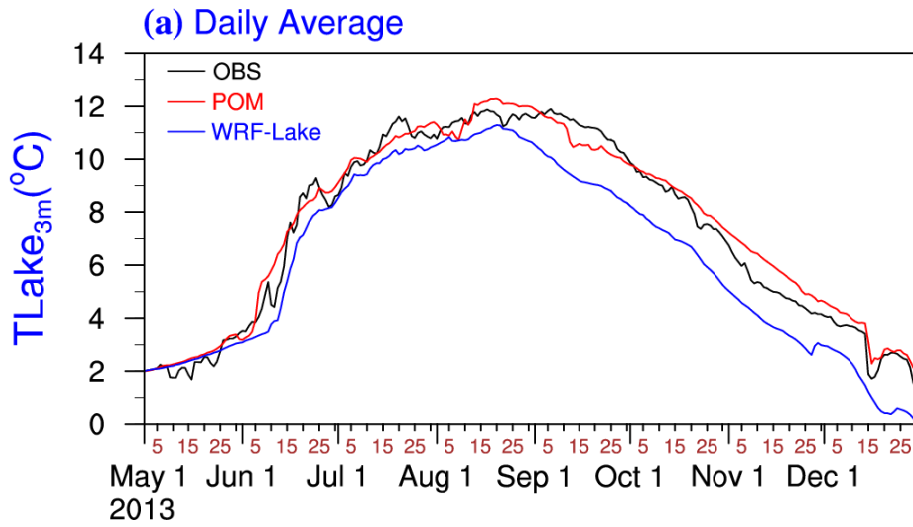
1026

1027 **Figure 1.** (a) Spatial distribution of the topography (unit: m) and lakes over central TP; (b) the
 1028 1-km POM/WRF-Lake grid bathymetry of LNC (unit: m). The purple and red asters represent
 1029 the water temperature site and the weather station, respectively. The dashed line denotes the
 1030 southwest-northeast transection used in Figures 8 and 9.



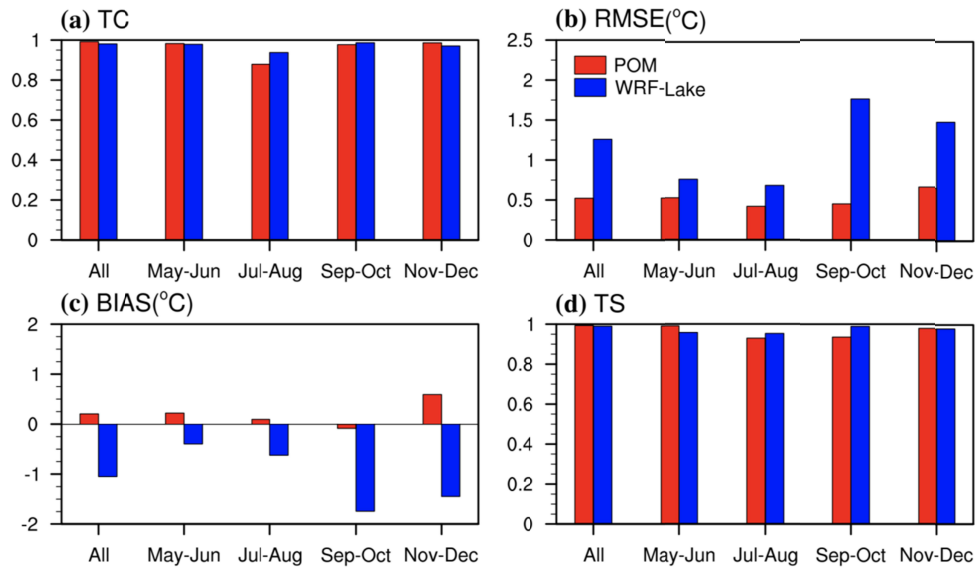
1032

1036 **Figure 2.** The daily in-situ (black lines) and CMFD (red curves) surface downward shortwave
 1037 radiation(a), downward longwave radiation (b), 2-m air temperature (c), 10m relative humidity
 1038 (d), and 10m wind speed (e) during 1th May to 31st December 2013. The blue line in (e) denotes
 1039 the calibrated wind speed by piecewise linear regression.



1037

1039 **Figure 3.** The daily $TLake_{3m}$ from the station measurements, the POM and WRF-Lake
 1040 simulations at the observation site during 1th May to 31st December 2013.



1040

1042 **Figure 4.** (a) TC, (b) RMSE, (c) BIAS, and (d) TS between the POM/WRF-Lake modelled
 1043 and observed daily $TLake_{3m}$ during the whole and bimonthly simulation periods.

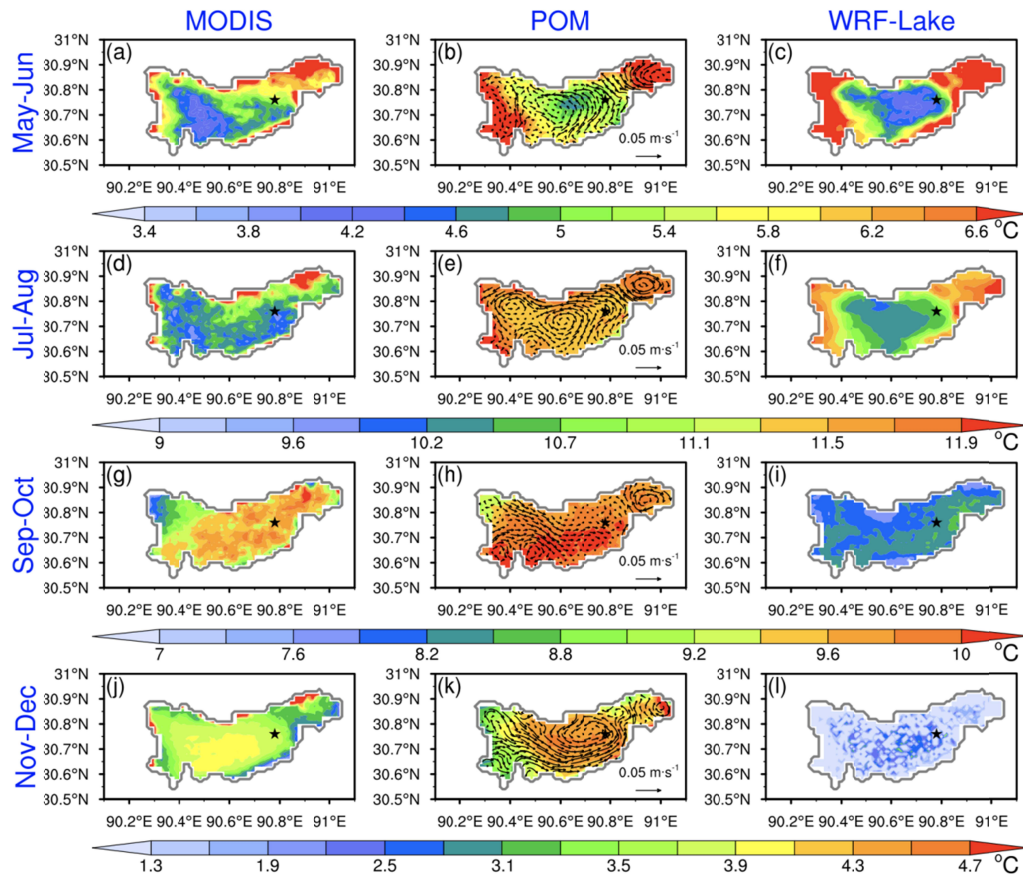
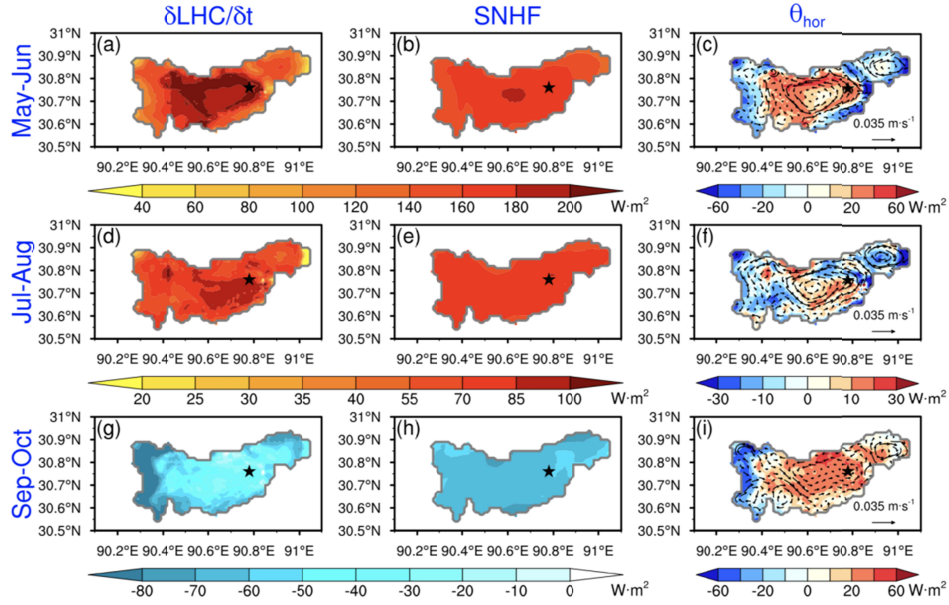


Figure 5. (a) MODIS retrieved, (b) POM, and (c) WRF-Lake simulated bimonthly averaged LST over the LNC during May-December 2013. The vectors in the middle panel represent the water currents averaged over the surface layers (0-3m). The black asters denote the water temperature site.



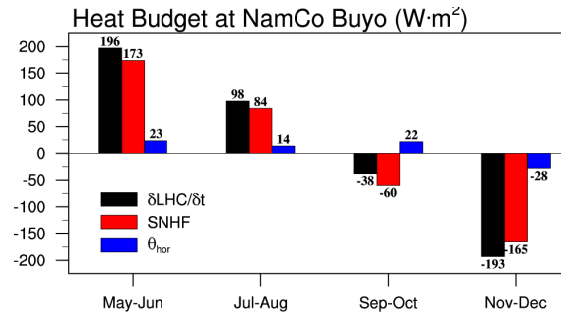
1051

1054

1055

1056

Figure 6. The bimonthly averaged heat budget components: rate of change in lake heat content $\delta LHC/\delta t$, surface heat flux SNHF, and horizontal heat exchange θ_{hor} (all units: $W \cdot m^{-2}$) over LNC during 2013. All the above variables are calculated based on POM results.



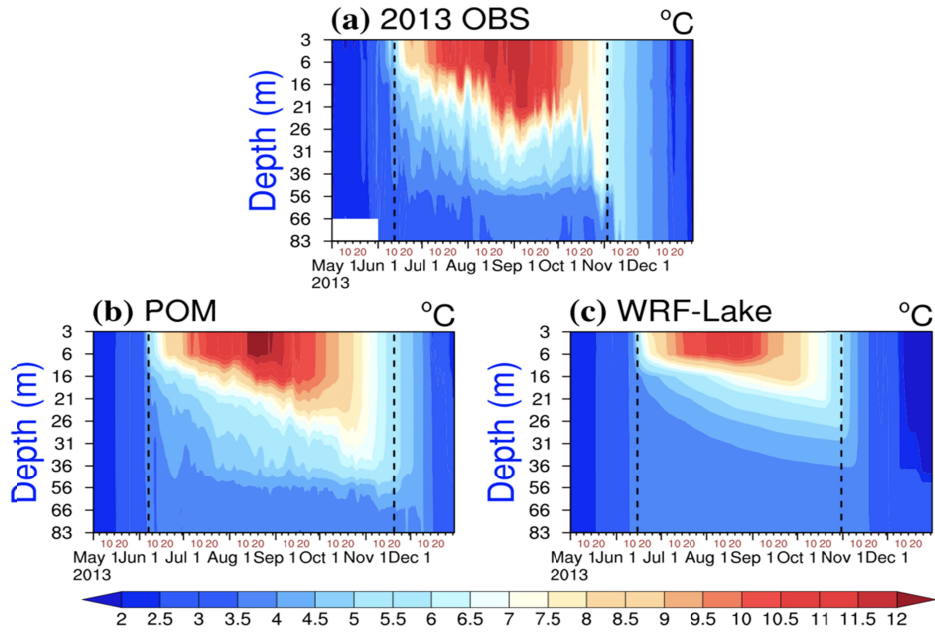
1055

1056

1057

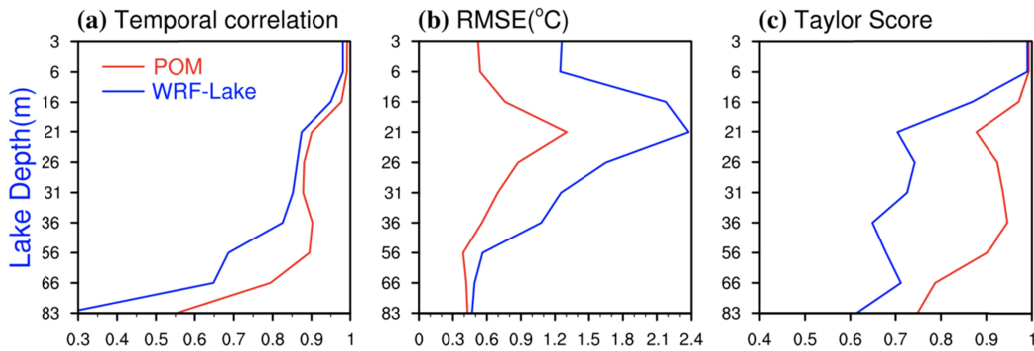
1058

Figure 7. Same as Figure 6, but for the heat budget at the water temperature site over LNC.



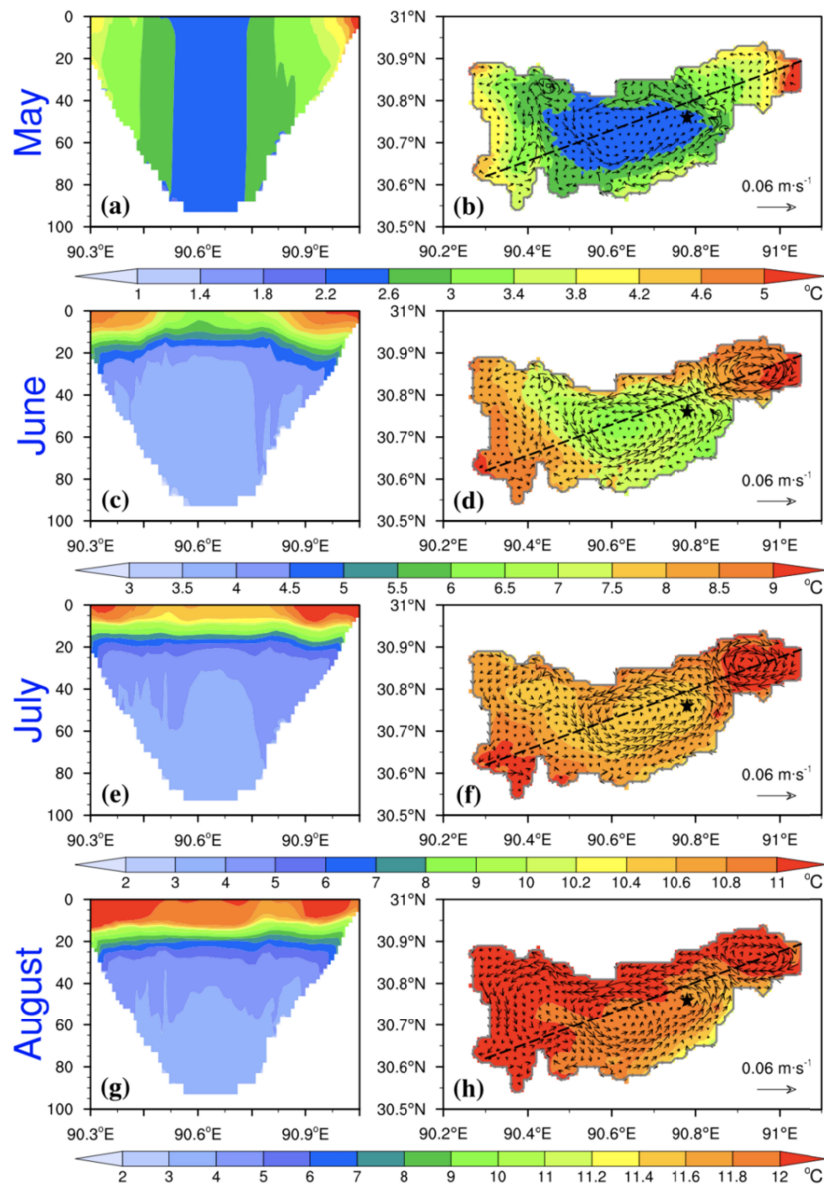
1059

1062 **Figure 8.** Time-depth distributions of the daily mean lake temperature from (a) the observation,
 1063 (b) POM, and (c) WRF-Lake simulations at the water temperature site during 1th May to 31st
 1064 December 2013. The black dashed lines indicate the onset and end of lake thermal stratification.



1063

1065 **Figure 9.** The vertical distributions of the (a) TC, (b) RMSE, and (c) TS for the daily mean lake
 1066 water temperature simulated by POM/WRF-Lake against the 10-layer in-situ observations.



1066

1070 **Figure 10.** Monthly averaged (a, c, e, g) lake temperature along the southwest-northeast
 1071 transection, (b, d, f, h) LST and depth-averaged currents over LNC during May-August 2013. In
 1072 (b, d, f, h), the black dashed lines denote the transection and the black solid asterisks represent the
 1073 location of Nam Co water temperature site.

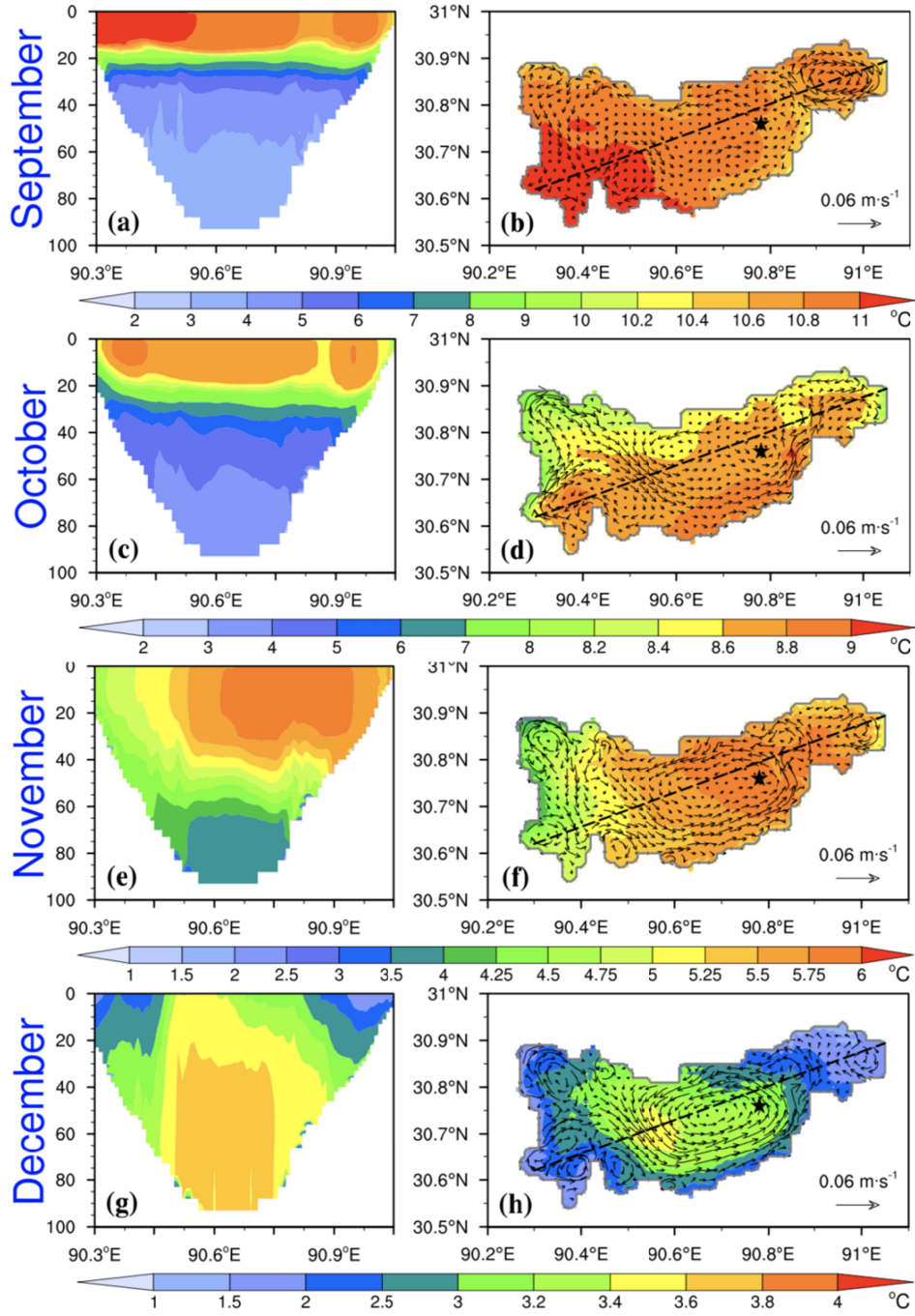


Figure 11. same as Figure 8, but for the period during September-December 2013.